CHAPTER 7

RESULTS AND DISCUSSION:

COLLOIDAL PROCESSING OF PZT CERAMICS AND THICK FILMS

In this chapter, the experimental results on the colloidal processing of both bulk PZT ceramics and PZT thick films are presented. For bulk ceramic processing, two colloidal processing techniques, i.e. viscous polymer processing (VPP) and direct coagulation casting (DCC) have been used in comparison with conventional dry powder pressing. The consolidation and sintering behaviour of the PZT ceramics produced using different processing routes and different powders are discussed in terms of their colloidal chemistry and powder characteristics. The dielectric and piezoelectric properties of the PZT ceramics are correlated with their microstructure and composition features. For the thick film processing, a colloidal processing technique, i.e. electrophoretic deposition (EPD) was used in comparison with conventional screen printing. The main issues encountered during the processing of PZT thick film are outlined.

7.1. Colloidal Processing of PZT Ceramics

7.1.1. Dispersion and Rheology of Aqueous PZT Suspension

7.1.1.1. Dispersion of PZT suspension

Fig. 7.1 shows the sedimentation behaviour as a function of pH (adjusted using HNO_3 (aq)) for a PZT suspension without dispersant. The PZT particles sediment very fast at pH 6.6, while the suspension becomes more stable under alkaline conditions, e.g. pH 9.0 and pH 10.4. However, when diammonium citrate (DAC) is added to the suspension as a dispersant, the suspension becomes relatively stable over a wider pH range of 5.1 to 10.3, except under strong acidic conditions, e.g. pH 3.5, as shown in Fig. 7.2. This is attributed to the different surface charge acquired by the PZT particles in aqueous suspension.

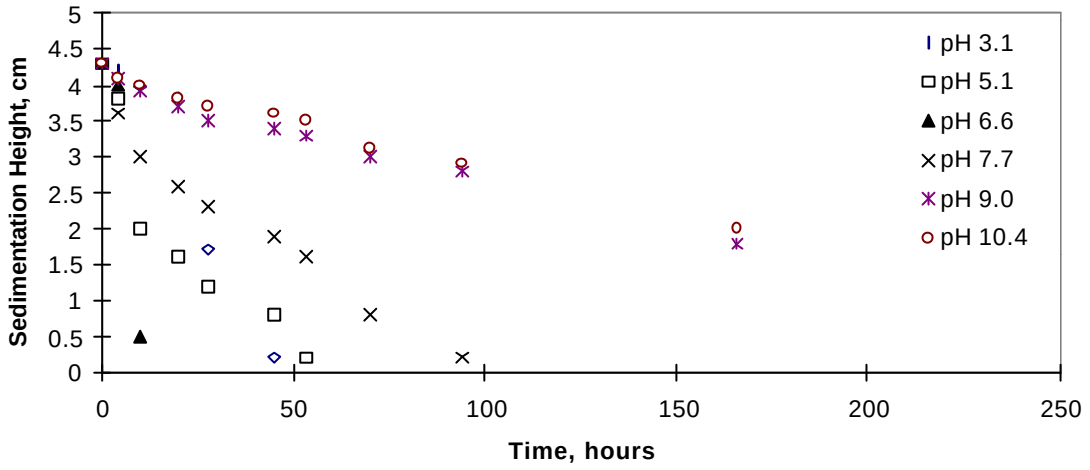

Fig. 7.1. Sedimentation height versus time for PZT-5A suspension without dispersant. Note the rapid sedimentation at pH 6.6.

Fig. 7.3 shows the electrophoretic mobility in relation to pH for PZT powders with and without dispersant. As can be seen, the isoelectric point (IEP) for PZT powder is at pH 6.5. Since the electrophoretic mobility is a measure of the electrostatic repulsion between particles in suspension [Hunter, 1971], a stable PZT suspension is expected either above pH 7 or below

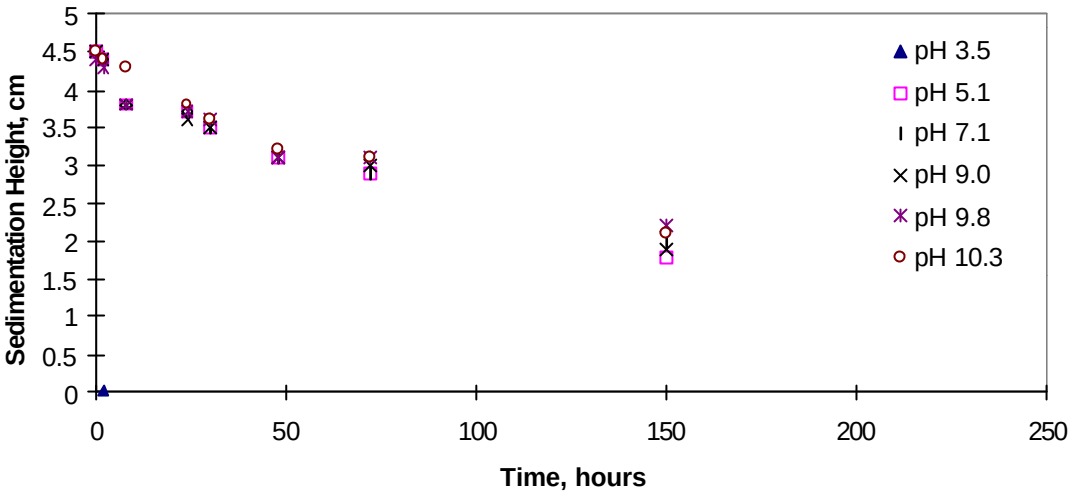

Fig. 7.2. Sedimentation height versus time for PZT-5A suspension with DAC of 0.25 wt. % of the PZT powders. Note that the suspension is stable at pH above 5.1.

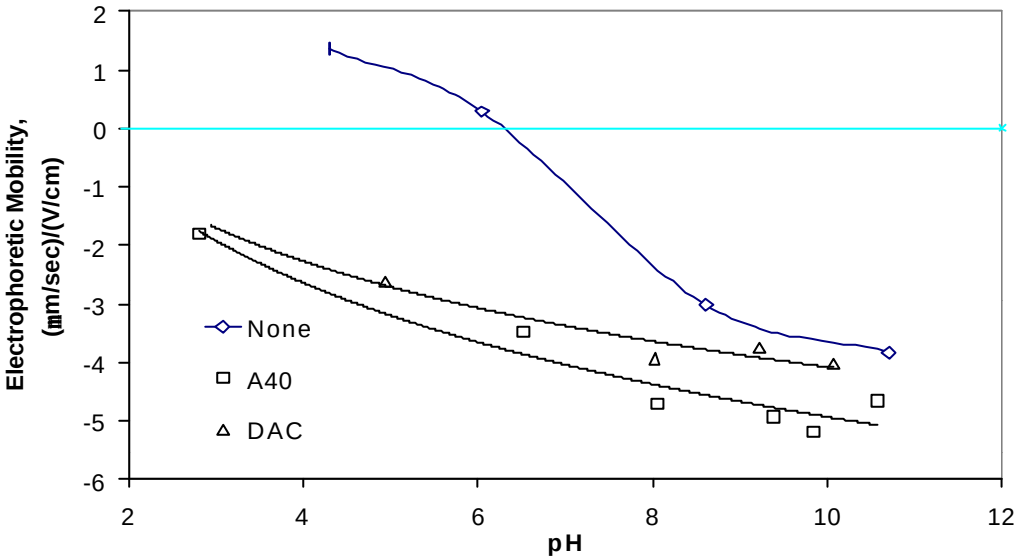

Fig. 7.3. Electrophoretic mobility versus pH curves for a hydrothermal PZT (HT-29) suspension with or without dispersant. The dispersant is diammonium citrate (DAC) and ammonium polycrylate

(A40), respectively. The solids loading of the suspension is 1 wt. %. The dispersant content is 0.5 wt. % of the PZT powder.

pH 6. At the IEP, however, PZT particles are expected to coagulate, thus leading to rapid sedimentation as shown in Fig. 7.1, because their net surface charge is zero. When DAC or an ammonium polyacrylate anionic polyelectrolyte (A40) is added to the PZT suspension, the surfaces of the PZT particles are altered significantly. As can be seen from Fig. 7.3, when DAC or A40 is used as a dispersant, both dispersants seem to be specifically adsorbed on the surfaces of the PZT particles, giving the particle surfaces a net negative charge. Therefore, the PZT suspension becomes more stable over a wide pH range (pH > 5.1) as shown in Fig. 7.2. It was reported that the citrate ($^-OOC)(OH)C(CH_2COO^-)_2$) is a potential-determining ion which can strongly adsorb to the hydroxylated oxide ceramic surface [Leong *et al.*,1993; Luther *et al.*, 1995]. This is because the citrate anion has three carboxyl (COO^-) groups and is therefore trivalent when fully dissociated; it can produce more negative charge to the surface relative to the number of positively charged surface sites it neutralises. For a given concentration, the citrate ions neutralise the existing positive surface sites and bring the surfaces with negative charge. It is also evident from Fig. 7.2 that the PZT suspension coagulates at pH 3.5 when DAC content is 0.25 wt.% of the PZT powders.

7.1.1.2. Viscosity of PZT suspension

The experimental results show that the stress-strain relationship for all the PZT suspensions in this study can be best described by the Herschel-Bulkley equation [Whorlow, 1992], i.e.

$$\tau = \tau_0 + k\gamma^n \quad (7.1)$$ where

τ is the stress, τ_0 is the yield stress, k is the viscosity coefficient, γ is the shear rate and n is the rate index (<1). This indicates that the PZT suspension must overcome a yield stress before it becomes shear shinning.

Taking the viscosity at a shear rate of 60 s^{-1} as the parameter for direct coagulation casting (DCC) processing, the viscosity of the PZT suspension with DAC versus the pH is shown in Fig. 7.4. For PZT suspensions with 0.25 wt. % DAC as a dispersant, the viscosity of the suspension was as low as 0.3 Pa.s over a broad pH range (pH >5.1), even at a solids loading of 50 vol. %. The rapid increase in the slurry viscosity of the slurry is probably due to the decrease in the net surface charge of the hydrothermal PZT powder as the pH decreased to <5, as shown in Fig. 7.3. However, when the solids loading increases, the viscosity increases drastically (Fig. 7.5). The maximum viscosity which allows mixing and casting is about 2 Pa.s at a shear rate of 60 s^{-1} [Graule *et al.*, 1995a]. Thus, PZT slurry with solids loading of 58 vol. % can be used for DCC processing.

7.1.2. Consolidation Behaviour

7.1.2.1. Direct coagulation casting (DCC)

The DCC-process is based on the destabilisation of a suspension by an internal chemical reaction. The products of internal reaction lead to the coagulation of a double-layer stabilised suspension by

minimising the double-layer repulsive forces, leading to a liquid-solid transition in a suspension. Reactions can be used, which either shift the pH of the stable suspension towards the IEP or which compress the double-layer by increasing the ionic strength of the suspension [Graule *et al.*, 1995a].

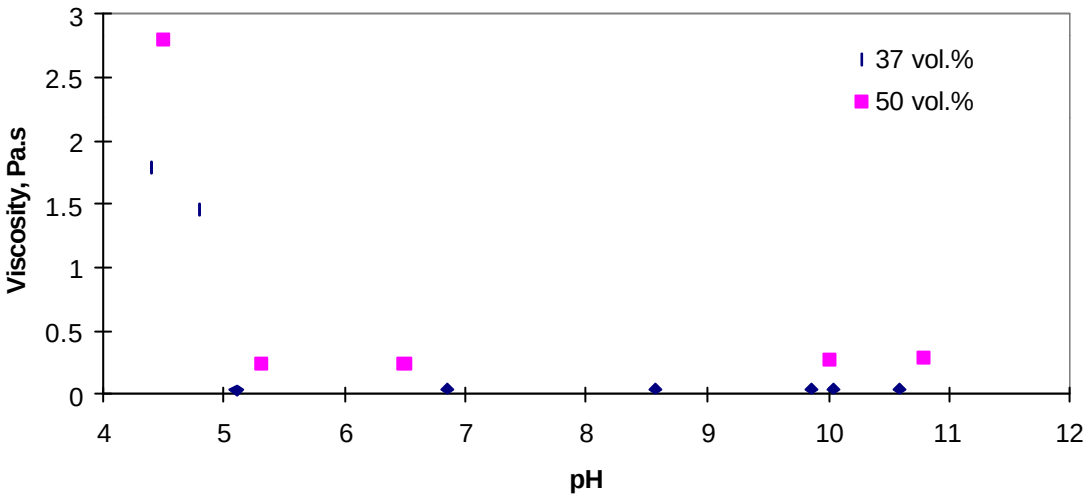

Fig. 7.4. Viscosity at a shear rate of 60 s^{-1} versus pH curves for PZT-5A slurries with a different solids loading. The suspensions are with a dispersant addition of DAC with 0.25 wt. % of the PZT powders. Note the low viscosity over a broad pH range.

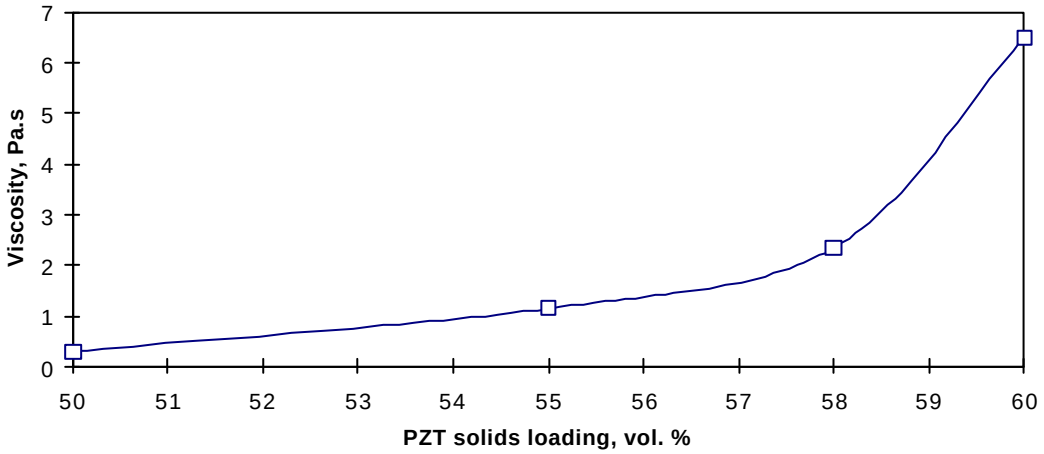

Fig. 7.5. Viscosity at a shear rate of 60 s^{-1} versus solids loading for PZT-5A slurries with 0.25 wt. % DAC as a dispersant at pH 5.1.

From the results and discussion in Section 7.1.1, for PZT suspension containing DAC as a dispersant, it is evident that coagulation will occur if the pH of the suspension shifts to pH < 5.1 (see Fig. 7.2 and 7.4). A lactone has been used in this study to bring about the internal change in the suspension pH. Fig. 7.6 shows the pH change of an aqueous δ-gluconolactone solution and a similar solution containing 1 wt. % DAC solution, respectively, at 20°C. The aqueous δ-gluconolactone solution pH changes rapidly from pH 6.5 to pH 2.5 within 5 minutes due to the self-hydrolysis of the lactone. However, in the weakly acidic DAC solution (pH 5.1), the δ-gluconolactone remains relatively stable against self-hydrolysis at 20°C, but the DAC solution pH nevertheless does change slowly with time and is accelerated by an increase in temperature (Fig. 7.7). This dual dependence on temperature and time makes it easier to control the coagulation behaviour of the suspension. PZT green bodies were made by this DCC-process route. However, cracks have been found in the green body probably because of its low coagulation strength owing to only limited pH changes by this hydrolysis reaction. In addition, leaching of lead is also possible because of the poor chemical resistance of PZT at low pH [Wen *et al.*, 1991].

Graule *et al.* [1995a, 1995b] reported another unique way of changing the solution pH or salt concentration by enzyme-catalysed reactions; namely, the decomposition of urea by urease (urea amidohydrolase):

$$(NH_2)_2CO + H_2O \xrightarrow{\text{urease}} 2\ NH_3 + H_2CO_3 \longrightarrow 2\ NH^{4+} + CO_3^{2-} \quad (7.2)$$

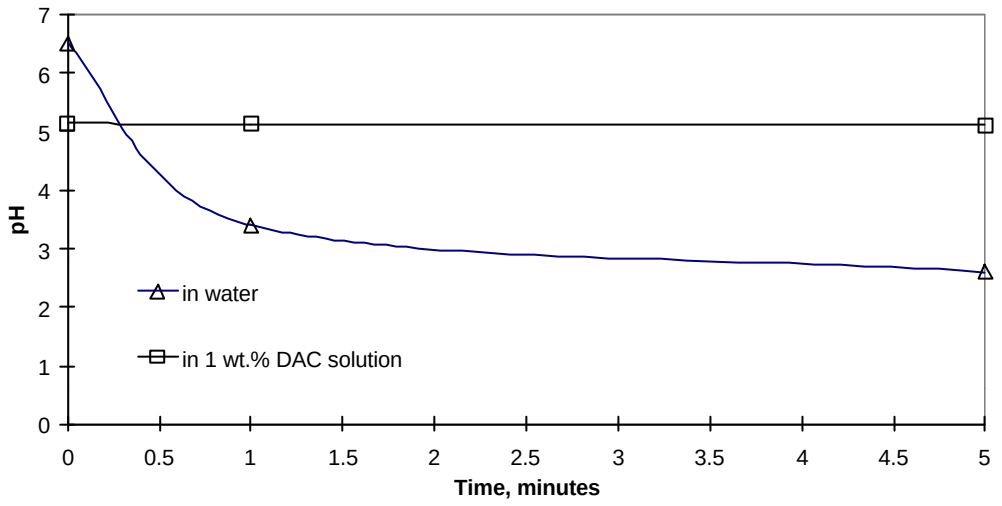

Fig. 7.6. pH changes with time for an aqueous δ-gluconolactone solution and that containing 1 wt. % DAC, respectively (at 20°C). Note the rapid hydrolysis of δ-gluconolactone in water.

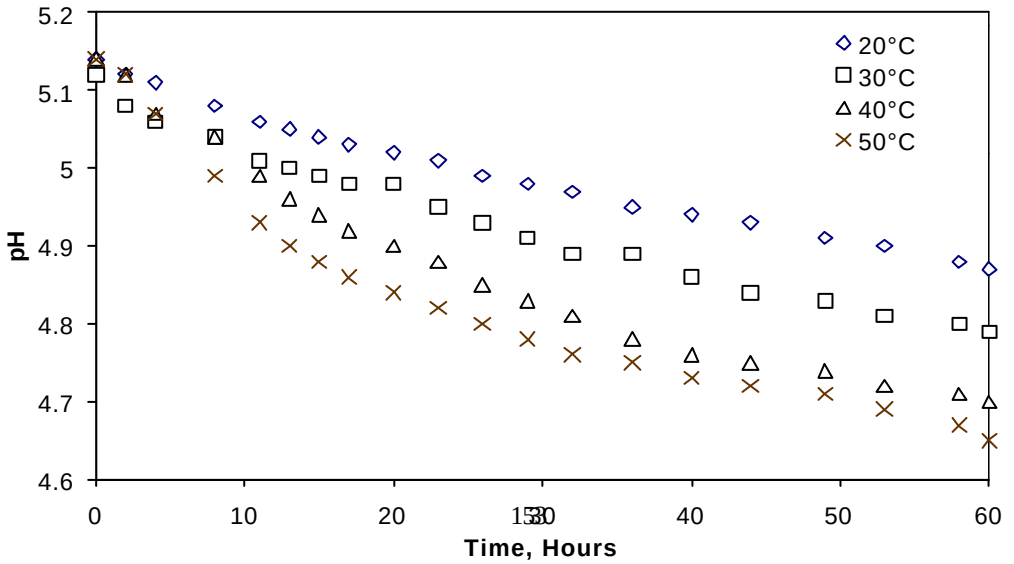

Fig. 7.7. pH versus time curves for δ-gluconolactone in 1 wt. % DAC solution at different temperatures, showing that the hydrolysis rate of δ-gluconolactone increases with temperature.

This reaction can shift the pH from 4 to 9 where diammonium-carbonate has its buffer point, which means that the pH will cease to change after reaching this point. Thus, when the reaction continues, it will increase the salt concentration. This is the second way to destabilise the suspension. It is sufficient to coagulate many suspensions when the salt concentration exceeds 1 M. Crack-free PZT green bodies with a high coagulation-strength have been made by this DCC-process route. Fig. 7.8 shows that the green density of the DCC-processed PZT compacts increases with the solids loading of the suspension. Air bubbles become entrapped in the green bodies when the solids loading is taken above 60 vol. % owing to the high viscosity.

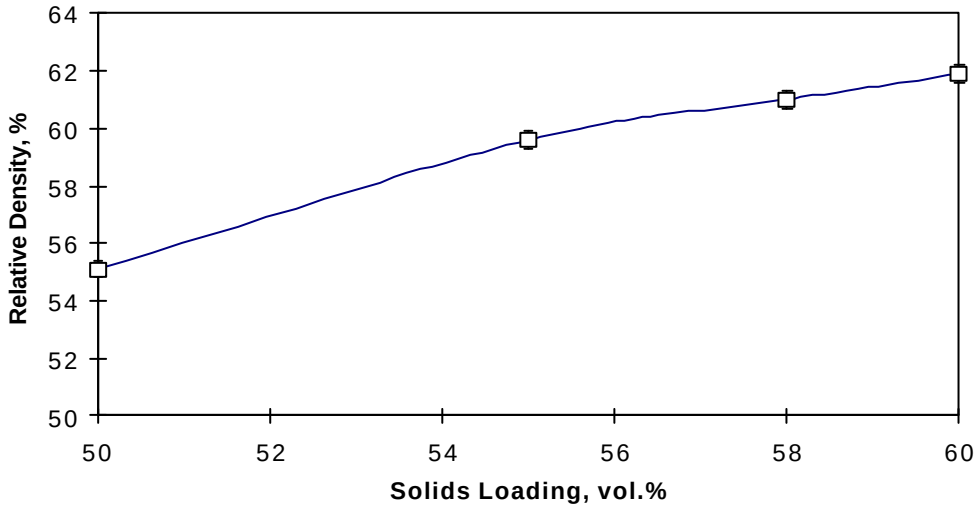

Fig. 7.8. Relative density (i.e. green density versus powder density) of the green body versus solids loading for PZT-5A ceramics processed via the DCC-process, using the urea/urease system at room temperature. The true powder density for PZT-5A is 7.8 g/cm^3 according to density bottle measurements.

However, a yellow and/or green thin film was formed on top of the green body when hydrothermal PZT powders were used for this process. This can probably be attributed to the less developed crystallinity and incomplete transformation of the hydrothermal PZT powders in comparison with the commercial mixed-oxide PZT-5A powder. The yellow material is probably the PbO (masicot) owing to leaching of Pb component from the hydrothermal PZT powder under current weak acidic conditions (pH 5.1).

7.1.2.2. Viscous polymer processing (VPP)

Viscous polymer processing or VPP involves the use of polymer solutions in a particular way in the processing of ceramic powders. It enables the powder agglomerates to be broken down more easily by using the viscous polymer solution to transfer significant stresses to the powder agglomerates, and also confers a number of benefits to the product such as better sintering behaviour, greater homogeneity and higher strength [Alford *et al.*, 1987; Kendall *et al.*, 1988].

The polymers used in this study are polyvinyl alcohol-acetate copolymer together with methyl cellulose. The former is a commonly-used binder in ceramic powder processing whose main function is to increase the green strength of the compacts by binding the powder particles together, while the latter is added to give the right visco-elastic behaviour in order to break down the agglomerates during the processing. Glycerol is used as a dispersant or lubricant. The experimental results show that the necessary polymer content is, however, strongly dependent on the powder characteristics. As can be seen from Table 7.1, the amount of polymer required to convert the hydrothermal PZT powder (HT-37) into a workable dough is almost twice that required for the mixed-oxide PZT powder (PZT-5A). This is because of the larger surface areas of the hydrothermal PZT powder particles. However, no significant difference between their green densities was evident after polymer burnt-out.

Table 7.1. Weight ratios for the dough compositions used in VPP of mixed-oxide (PZT-5A) and hydrothermal (HT-37) powders

	PZT-5A	**HT-37**
PZT powder	100	100
polyvinyl alcohol-acetate	3	6
methyl cellulose	2	2.5
water (containing 10 wt. % glycerol)	7	12

7.1.2.3. Comparison of VPP and DCC with uniaxial dry powder pressing

Fig.7.9 shows the relative density as a function of compaction pressure for green compacts of the PZT-5A and the hydrothermal (HS-36) powders produced by uniaxial dry powder pressing (see Section 5.2.1 for full details). The compaction density increases with applied pressure for both samples despite their different powder characteristics. However, the PZT-5A powder with its larger particle size and broader size distribution exhibits a higher green density than the HS-36 powder which has a narrower particle size distribution. Broad particle size distributions generally exhibit better particle packing and thus higher packing density because the voids between large particles can be filled by smaller particles [Bortzmeyer, 1995]. The SEM observations show that the smaller particles do fill in the voids between the larger particles in the case of the PZT-5A powder, yet some of the large voids appear to remain in the compacts of both powders (see Fig.7.10). Note that the microstructure of the HS-36 green compact is relatively uniform, with little particle agglomeration being evident from the polished surface. It is noteworthy that the green compacts processed via colloidal processing, either wet (DCC) or semi-wet (VPP), exhibit higher green densities than the dry pressed compacts, despite the applied pressure being lower (see Table 7.2). Particles in the colloidal state are much less resistant to rearranging and dispersion prevents further agglomeration, so a more uniform microstructure is achieved. This is attributed mainly to the modification of the interparticle forces by the added dispersant.

Table 7.2. Green density of the PZT ceramics produced by dry pressing, VPP and DCC

Processing	Dry Pressing	VPP	DCC
Green density of PZT-5A (g/cm^3)	4.59	4.80	4.84
Relative density of PZT-5A (%)*	58.8	61.5	62.1
Green density of HT-37 (g/cm^3)	3.81	4.07	-
Relative density of HT-37 (%)*	58.6	62.6	-

* The relative density is defined as the ratio of green density to powder density. The true powder density as measured by the density bottle method for PZT-5A and HT-37 was 7.8 and 6.5 g/cm^3, respectively.

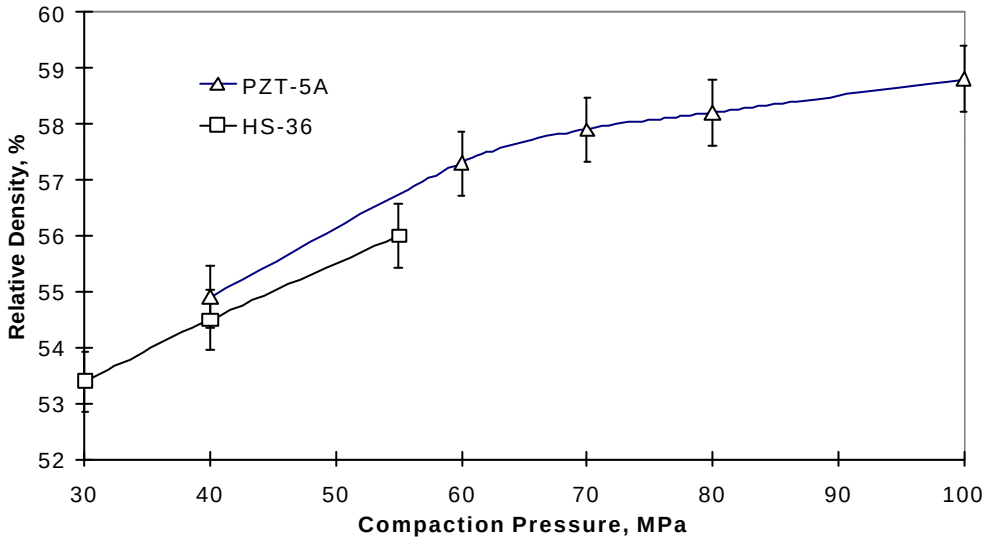

Fig. 7.9. Relative density versus compaction pressure for the green compacts produced by uniaxial dry powder pressing. The true powder density as measured by the density bottle method was 6.5 and 7.8 g/cm^3 for the HS-36 and PZT-5A powder, respectively.

Fig. 7.10. SEM micrographs of a polished surface, normal to the pressing direction axis, of green compacts of the PZT-5A (a) and the HS-36 (b) produced by uniaxial dry pressing, showing the different pore sizes and distributions for the two powders. 7.1.3. Sintering Behaviour

7.1.3.1. Densification during sintering

Fig. 7.11 shows the sintered density versus sintering temperature curves for both hydrothermal and mixed-oxide PZT powders processed via dry pressing and VPP routes respectively and sintered for a fixed time of 2 hours. The benefits of using colloidal processing (VPP) and smaller sized hydrothermal powders are clearly evident. The sintering temperature for the hydrothermal HT-37 powder is significantly lower (about 250°C) than that for the mixed-oxide PZT-5A powder. Also,

the sintering temperature for the VPP-processed ceramic is about 100-150°C lower than that for the dry-pressed ceramic. For HT-37 with a finer particle size and narrower particle size distribution, the sintered density increases abruptly in the sintering temperature range of 750 to 900°C, whereas for PZT-5A powder, it increases gradually and reaches the maximum at temperatures significantly higher than that for HT-37. The dilatometry data for the two different powders show that the shrinkage of the HT-37 reaches completion within a very narrow temperature range (<100°C), while for PZT-5A powder, this process is very slow, and has not finished, even at temperatures as high as 1300°C (see Fig. 7.12). The shrinkage for the former is also significantly larger than that for the latter. The results indicate that the hydrothermal PZT powder can be sintered to almost full density within a very short time.

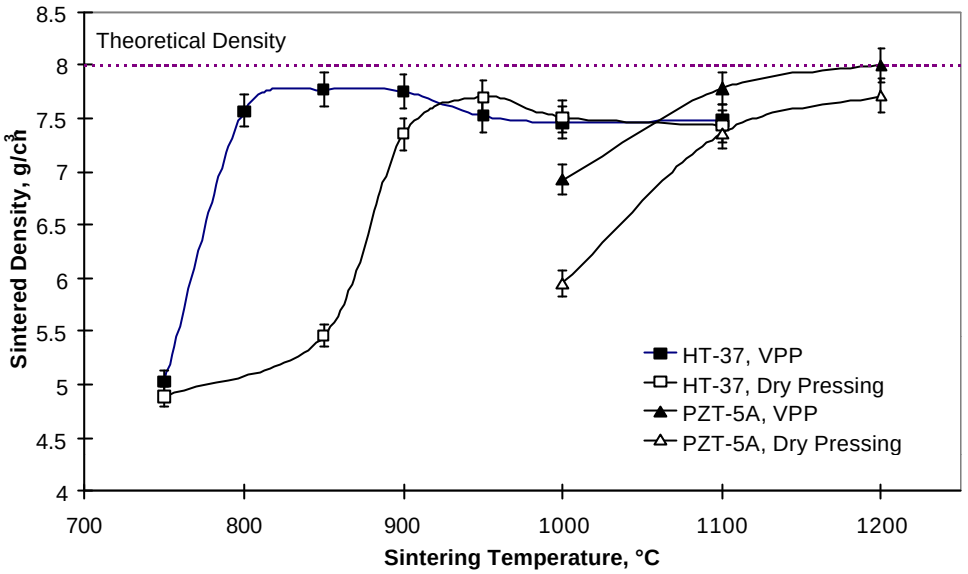

Fig. 7.11. Sintered density versus sintering temperature (for a fixed time of 2 hours) for both hydrothermal (HT-37) and mixed-oxide (PZT-5A) ceramics, produced by VPP and by dry pressing.

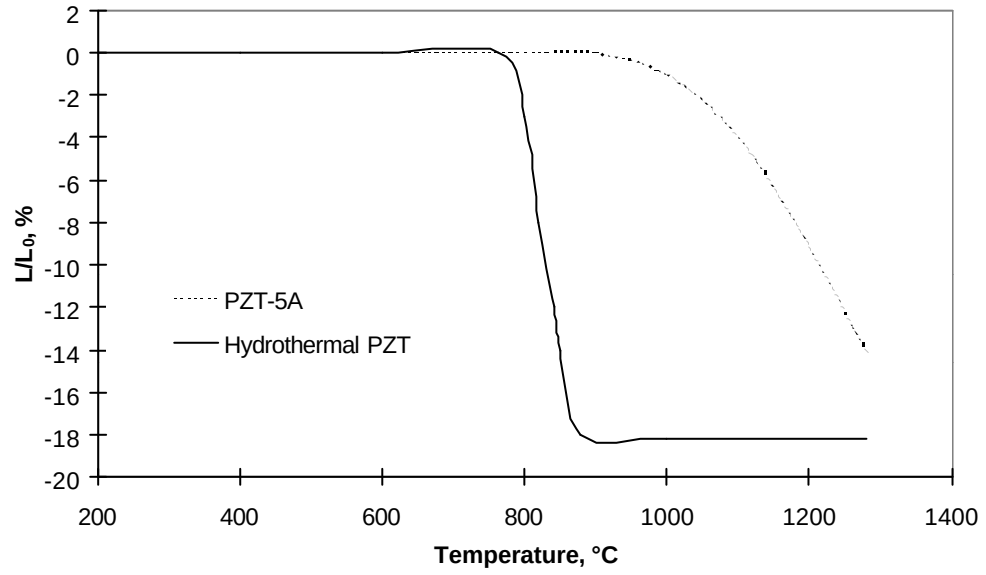

Fig. 7.12. Dilatometry data for the mixed-oxide PZT-5A and hydrothermal (HT-37) PZT powders, showing the % linear shrinkage as a function of temperature.

Fig. 7.13 shows the variations in sintered density, linear shrinkage and weight loss with the sintering temperature at a fixed sintering time of 5 minutes. It can be seen that the results are consistent with those in Fig. 7.11 and Fig. 7.12. The sintered density of the hydrothermal PZT powder (HT-29) increases rapidly at a temperature below 850°C, reaching the maximum at 850°C, and then decreases slightly with the sintering temperatures. It is noticeable that the weight loss of HT-29 increases with increasing sintering temperature correspondingly. Surprisingly, the weight loss of PZT-5A is negligibly low over the whole sintering temperature range, though its sintered density is only 95% of the theoretical at 1200°C, almost the same as that of the HT-29.

The origin of the weight loss for hydrothermal PZT green compact can be divided into two parts as shown in the TGA-DTA curve (Fig. 7.14). The first weight loss between 220°C and 330°C arises from the unreacted organic groups such as the acetate group, which are still bound to the Zr or Ti atoms, as discussed in Section 6.3, and hence, are difficult to eliminate completely during hydrothermal synthesis, even after heat-treatment at temperatures as high as 600°C. Note that both the dry-pressed and VPP-processed green compacts were subject to debinding at 600°C for 2 hours prior to sintering. The second weight loss above 900°C corresponds to lead oxide evaporation [Hardtl and Rau, 1969]. In comparison, the mixed-oxide PZT-5A green compact exhibits only the second weight loss and the onset temperature for lead loss is about 100°C higher than that for HT-37. The weight loss above 900°C is equally rapid for both materials. Therefore, the weight losses

during sintering have arisen mainly from lead oxide evaporation. Table 7.3 shows that a lower weight loss during sintering is observed when the PZT powders synthesised hydrothermally either at higher synthesis temperatures, for longer times or using a mineraliser concentration higher than the critical one. These experiments indicate that the overall weight loss could be related to the crystallinity of the PZT powders. Increasing the crystallinity of the hydrothermal PZT powders can suppress the weight loss due to the lead oxide evaporation during the sintering process. But the negative consequence of this is that the sintering temperatures have to increase owing to the increased particle sizes under these synthesis conditions as discussed in Section 6.2.

Table 7.3. Weight loss (%) of the PZT ceramics made from different hydrothermal powders after sintering at 1200°C for 2 hours.

Hydrothermal PZT Powder	HT-22	HT-24	HT-26	HT-27
Mineraliser (NaOH) Concentration (M)	0.3	0.5	0.3	0.3
Synthesis Temperature(°C)/Time (hours)	300/2	300/2	350/2	300/6
Weight Loss (%) After Sintering at 1200°C/ 2 hours	3.5	1.2	1.0	1.6

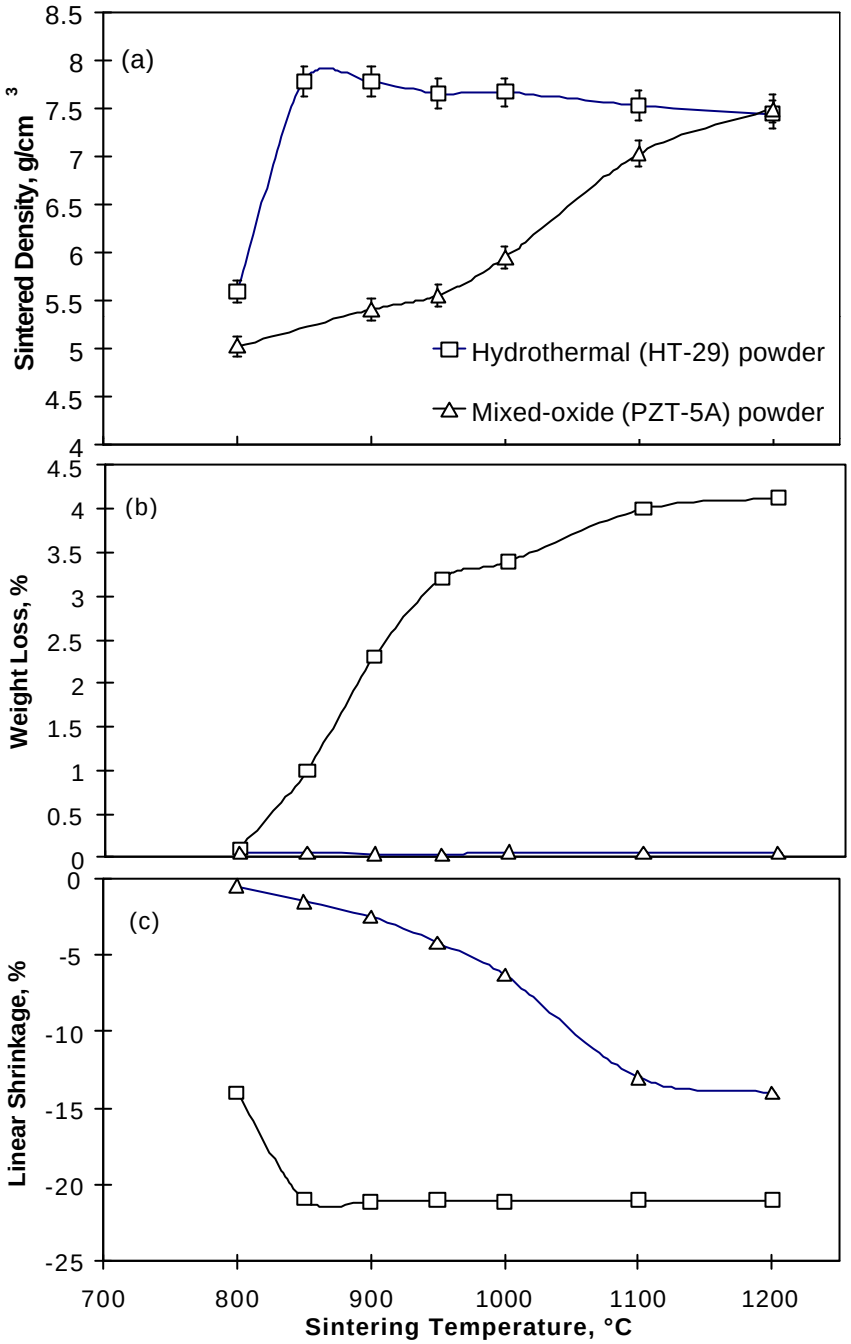

Fig. 7.13. Sintered density (a), weight loss (b) and linear shrinkage (c) versus sintering temperature at a fixed sintering time of 5 minutes for the dry-pressed hydrothermal (HT-29) and mixed-oxide (PZT-5A) ceramics.

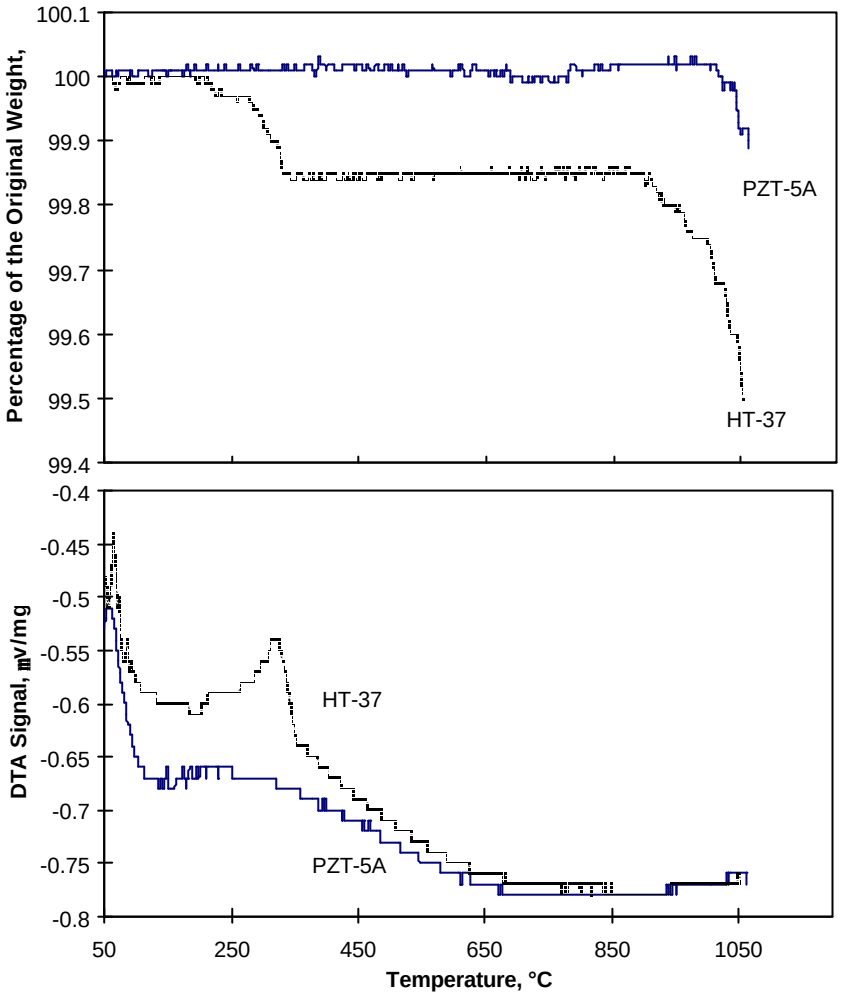

Fig. 7.14. TGA-DTA curves (at a heating rate of 10°C/min) for the hydrothermal HT-37 and mixed-oxide PZT-5A green compacts.

7.1.3.2. Microstructural evolution during sintering

The series of SEM micrographs of the fracture surfaces shown in Fig. 7.15 illustrate successive stages of the microstructural evolution during the sintering of uniaxially dry pressed compacts of both mixed-oxide (PZT-5A) and hydrothermal (HT-29) PZT powders.

At a sintering temperature of 750°C, the microstructure for both PZT-5A and HT-29 powders exhibits little change in comparison with their state in the green compacts. The HT-29 powder with a finer particle size exhibits some coarsening without too much agglomeration (Fig. 7.15 (b)), whereas the PZT-5A powder possesses some large particles and/or agglomerates surrounded by smaller particles (Fig. 7.15 (a)), a typical feature for jet-milled ceramic powders. When the sintering temperature is increased to 850°C, a tremendous change occurs in the HT-29 ceramic where sintering takes place rapidly with distinct grain boundaries being visible on the fracture surface (Fig. 7.15 (d)), while for PZT-5A, only some regions of particle agglomeration, where the smaller particles surround larger ones, begin sintering (Fig. 7.15 (c)). At this temperature, the density of the HT-29 increases markedly compared with that of the PZT-5A (see Fig. 7.13). As the sintering temperature is increased to 1000°C, the grain size of the HT-29 ceramic doubles from about 1 μm at 850°C to about 2 μm at 1000°C (Fig. 7.15 (f)), with the densification taking place via conventional solid-state sintering, governed by either lattice diffusion or grain-boundary diffusion. In contrast, the PZT-5A ceramic still undergoes intra-agglomerate sintering (Fig. 7.15 (e)). Its sintered density is still quite low (about 75 % theoretical). Finally, at a sintering temperature of 1200°C, the PZT-5A ceramic has sintered with clear grain boundaries on its fracture surface (Fig. 7.15(h)) with its density increasing to 93 % theoretical (Fig. 7.13), whereas the grain size of the HT-29 ceramic has increased to about 2.8 μm (Fig. 7.15 (g)). The difference in the microstructure evolution between the hydrothermal HT-29 powder and the mixed-oxide PZT-5A powder is attributed to their different particle characteristics (see Fig. 7.16). As a result, the two ceramics exhibit entirely different sintering behaviour.

Fig. 7.17 shows the series of SEM micrographs of polished surfaces of the PZT-5A and another hydrothermal PZT powder, HS-36, which was synthesised at 200°C for 30 minutes using 4 M KOH as a mineraliser, together with the one-step derived feedstock. As can be seen from Fig. 7.16, the average particle size for HS-36 (1 μm) are larger than that for PZT-5A (0.8 μm), but the PZT-5A exhibits a broader particle size distribution. At a sintering temperature of 1000°C, for the PZT-5A powder, the regions comprising particle agglomerates, where the smaller particles are surrounding larger ones have sintered first (Fig. 7.17(a)). The PZT-5A powder with its smaller particle size portion shows a more significant effect on intra-agglomerate sintering. The difference in the agglomerate sizes becomes even more noticeable in the partially-sintered microstructures at a sintering temperature of 1100°C; see Fig. 7.17 (c). At this temperature, the partially-sintered microstructure of the HS-36 ceramic seems to be less developed than the PZT-5A. Finally, when the sintering temperature is raised to 1250°C, the density has increased dramatically for both ceramics. However, the microstructural change in the HS-36 ceramic is significant. The densification occurs rapidly for the HS-36 ceramic.

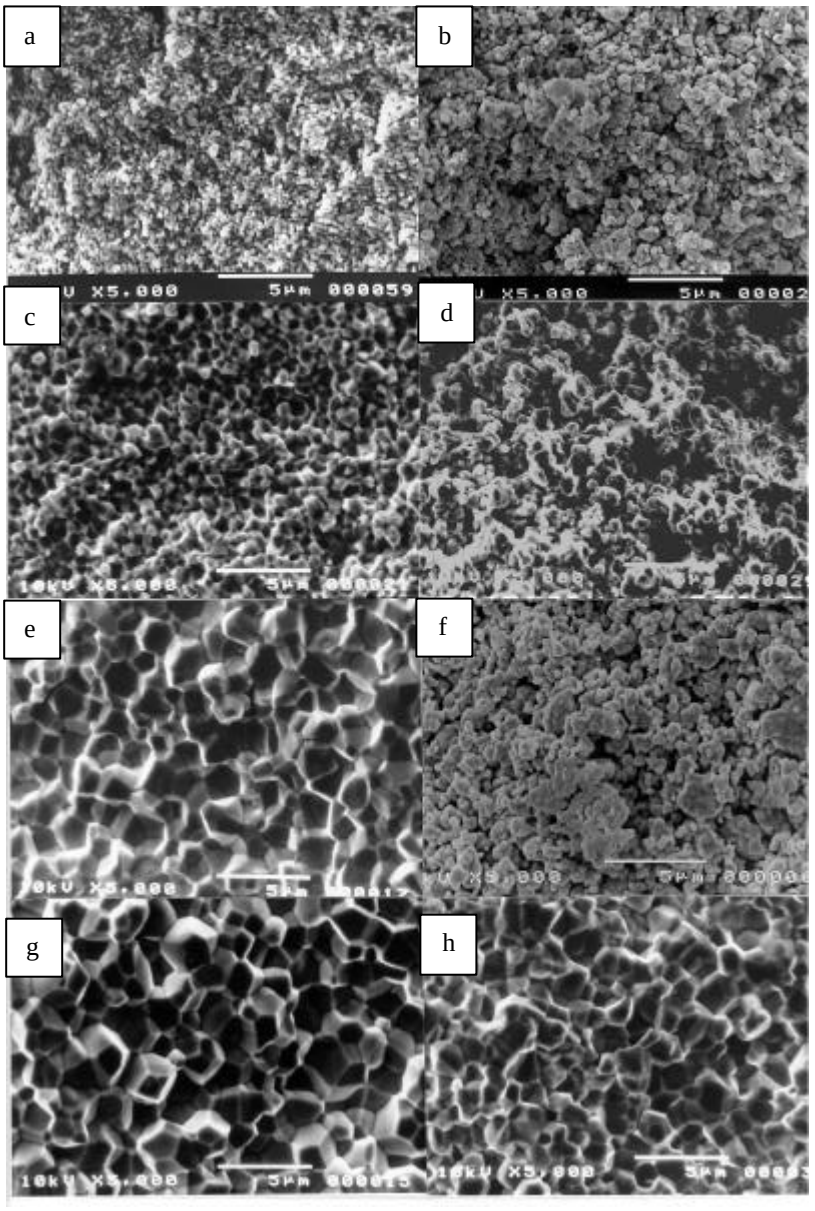

Fig. 7.15. SEM micrographs of the microstructural evolution of the fractured surfaces of PZT-5A (left) and HT-29 (right) ceramics during sintering showing the different sintering behaviour of PZT compacts under the same sintering conditions of (a), (b) 750°C; (c), (d) 850°C; (e), (f) 1000°C; and (g), (h) 1200°C for 2 hours, corresponding to the different powder characteristics.

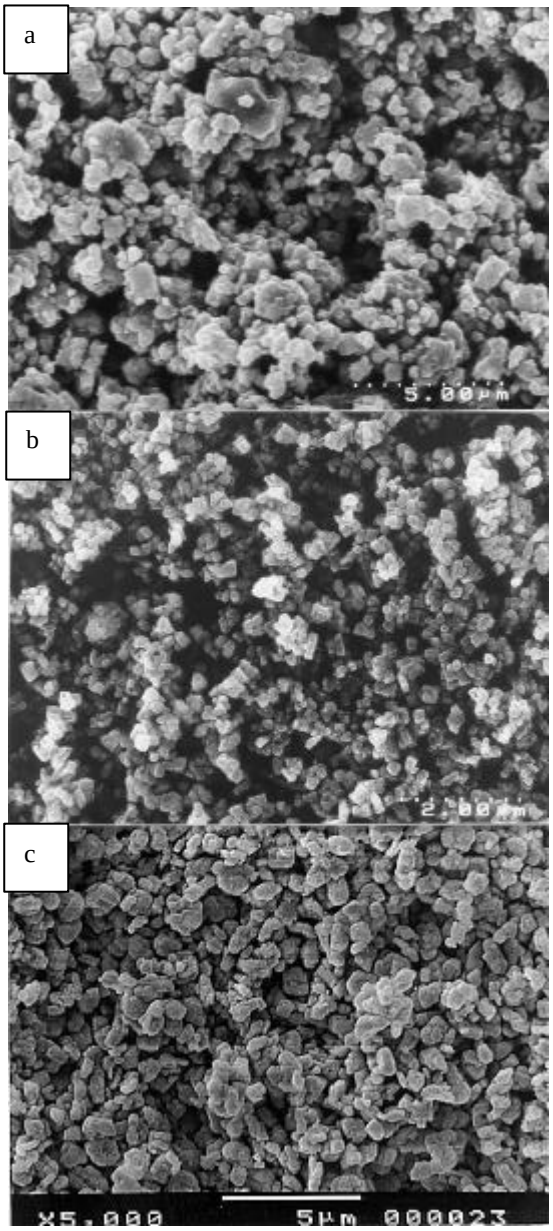

Fig. 7.16. SEM micrographs of the PZT powders: (a) mixed-oxide PZT-5A; (b) hydrothermal HT-29; and (c) hydrothermal HS-36 powder. Note that each powder exhibits a different particle size distribution and morphology.

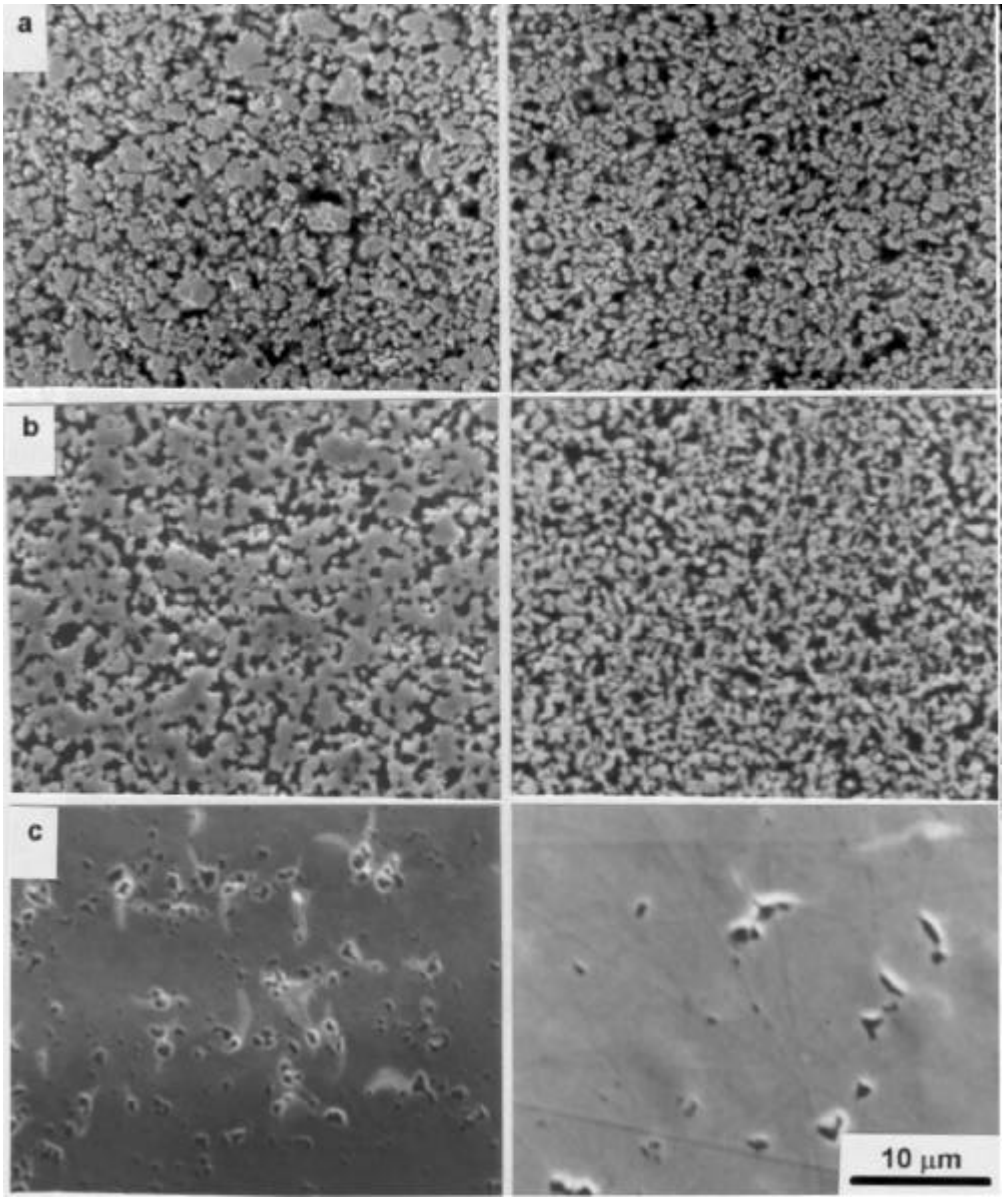

PZT-5A HS-36

Fig. 7.17. SEM micrographs of the microstructural evolution of PZT-5A (left) and HS-36 (right) ceramics during sintering showing the different sintering behaviour of PZT compacts under the same sintering conditions of (a) 1000°C; (b) 1100°C; and (c) 1250°C for 1 hour, corresponding to the different powder characteristics.

Fig. 7.18 shows the SEM micrographes of the polished surfaces of the PZT-5A and HS-36 ceramics after thermal etching treatment. It is interesting to note that the thermal etching conditions have a marked effect on the appearance of the grain boundaries of the PZT ceramics due to the volatilisation of PbO at temperatures above 800°C. The SEM micrographs in Fig. 7.18 (a) and (c) show that after thermal etching in air, the grain boundary structure is quite evident in the PZT-5A sample (Fig. 7.18 (a)). In contrast, the HS-36 sample exhibits a porous structure with no distinct grain boundary structure (Fig. 7.18 (c)). However, when thermally etched under the same conditions but in a PbO atmosphere buffer, both samples exhibit distinct grain boundary structures (see Fig. 7.18 (b) and (d)). Under the latter conditions, PbO evaporation is greatly suppressed; thus, these results are consistent with the previous observation that the PZT-5A ceramic is more stable against PbO loss.

The effect of sintering atmosphere is shown in Fig. 7.19. A higher sintered density and lower weight loss were observed for both the PZT-5A and HS-36 ceramics when sintered at 1250°C for 1 h in oxygen rather than in air. This is probably due to the higher O_2 partial pressure, which suppresses the PbO volatilisation as shown by the lower weight loss in Fig. 7.19, and reduces the rate of grain growth as evident from Fig. 7.20. At higher grain growth rates, pores become trapped within grains, whereas at slower rates, the pores can diffuse out to the boundaries and be eliminated [Ogawa, 1991].

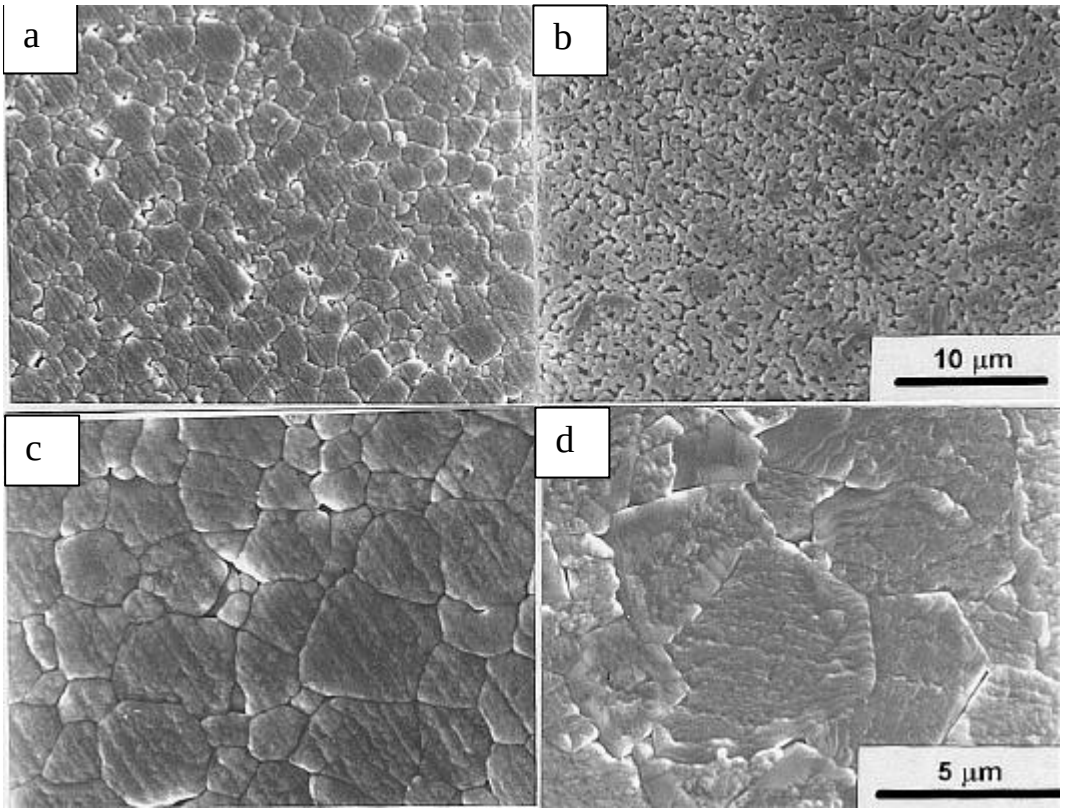

PZT-5A HS-36

Fig. 7.18. SEM micrographs of the thermally etched surfaces normal to pressing direction axis of the PZT ceramics subjected to different atmospheres at 1000°C for 1 minute: (a) PZT-5A, air; (b) PZT-5A, PZT buffer; (c) HS-36, air; and (d) HS-36, PZT buffer. Etching is clearly more severe in air.

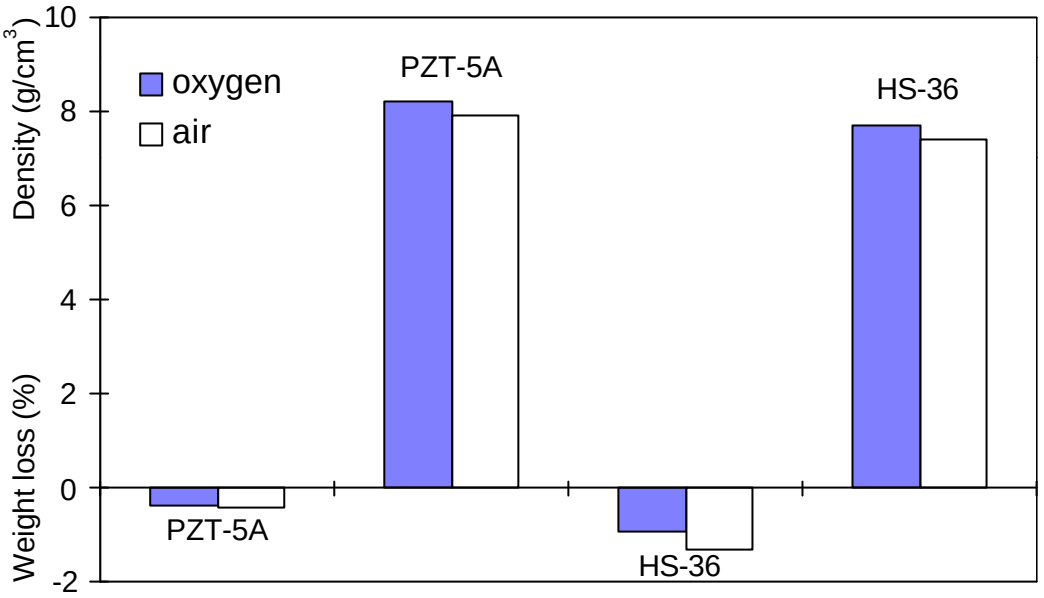

Fig. 7.19. Weight loss and density of the PZT-5A and HS-36 powders when sintering in different atmospheres.

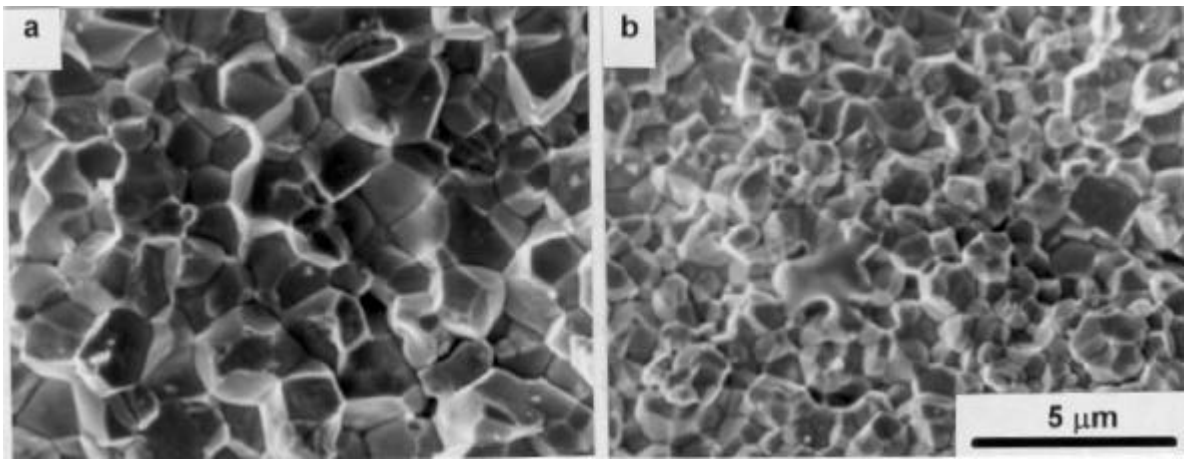

Fig. 7.20. Fracture surface of the PZT-5A ceramic sintered at 1250°C for 1h in (a) air and (b) an oxygen atmosphere. Note the larger grain size on sintering in air.

7.1.3.3. Phase development during sintering

The phase development of the ceramics from both hydrothermal (HT-37) and mixed-oxide (PZT-5A) PZT powders during sintering is shown in Fig. 7.21. The coexistence of tetragonal and rhombohedral phases is observed for both powders as indicated by the (200) reflection in the XRD patterns ($2\theta = 43\sim46^\circ$). There are three peaks for the initial powders, i.e., $(200)_t$, $(200)_r$ and $(002)_t$, showing that the composition of both powders is near the morphotropic phase boundary (MPB) in the solid-solution $PbZrO_3$-$PbTiO_3$ phase diagram [Ari-Gur and Benguigui, 1975]. But the peaks are broader for the HT-37 powder, showing less homogeneity in the as-synthesised hydrothermal PZT powder under the present synthesis conditions. As discussed in Section 6.3, the hydrothermal PZT powders synthesised at the critical mineraliser concentration actually comprise a mixture of PZT (T) and PZT (R) phases. On sintering at 800°C, the XRD pattern for the PZT-5A ceramic remains unchanged, whereas the peaks in the XRD pattern for the HT-37 ceramic have become narrower, indicating that a homogenisation process is occurring during the initial sintering stage. As the sintering temperature increases, the peaks at (200) reflection for the HT-37 ceramic split into two peaks (i.e. $(200)_t$ and $(002)_t$) for the tetragonal structure [Hahn *et al.*, 1978; Mabud, 1980] (see Fig. 7.21 (a)); this peak split is less obvious for the PZT-5A ceramic (see Fig. 7.21 (b)). The shift in the crystal structure of the PZT ceramic from tetragonal/rhombohedral to tetragonal is believed to be caused by the evaporation of lead oxide, resulting in the precipitation of ZrO_2, which moves the composition from the MPB towards the ZrO_2-PZT region [Ikeda *et al.*, 1962]. Although the ZrO_2 reflection is not shown in the XRD pattern for the bulk PZT ceramics, probably because its content is well below the XRD detection limit (< 5 mol. %) or its crystal size is too small (< 10 nm), it is clearly evident in

the XRD patterns of PZT films given in Section 7.2.2, where the lead oxide evaporation is more severe due to the large surface area. Furthermore, the weight loss of the PZT-5A during sintering is much less than that of the HT-37 as stated already; the splitting of the peaks in the XRD pattern is less obvious. A similar result is found for the hydrothermal PZT powders synthesised using a relatively high mineraliser concentration of 2 M KOH. Fig. 7.22 shows that the crystal structure of the HS-6 powder which was synthesised using 2 M KOH as the mineraliser, changes to the tetragonal form after sintering at 1250°C, whereas the HS-36 powder which was synthesised using 4 M KOH as the mineraliser, remains in the rhombohedral form after sintering. This is attributed to the latter powder having a well crystallised structure which is much more stable against lead loss during sintering.

7.1.3.4. Enhanced sintering mechanisms

The process of sintering does not usually involve only a single mass transport mechanism. During the sintering of most ceramics, more than one mechanism is operating. Basically, there are two classes of mass transport mechanisms; namely, surface transport and bulk transport. Each class is composed of several actual atomic mechanisms contributing to mass flow [German, 1996].

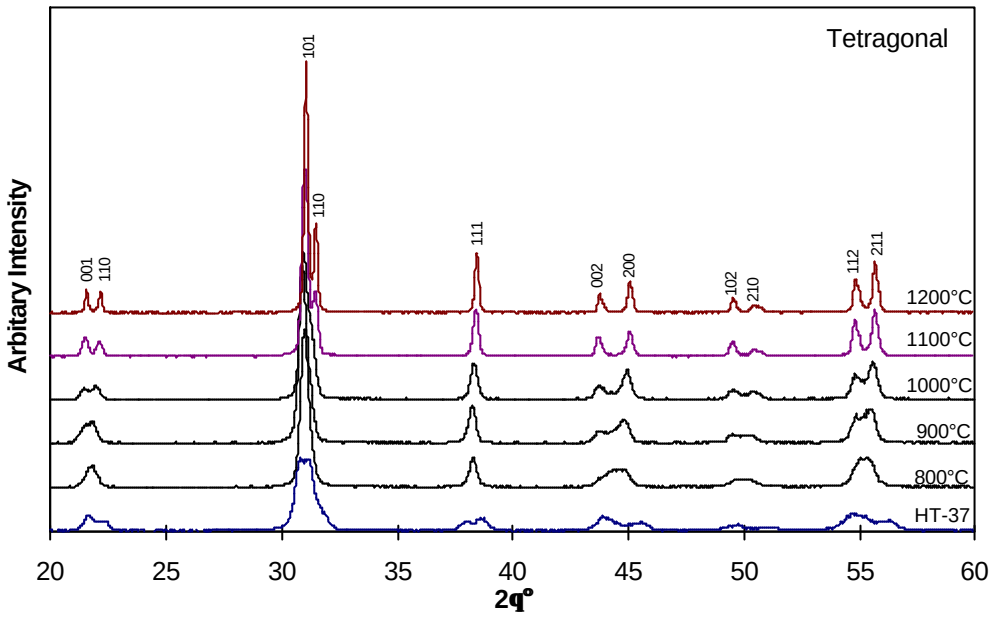

(a)

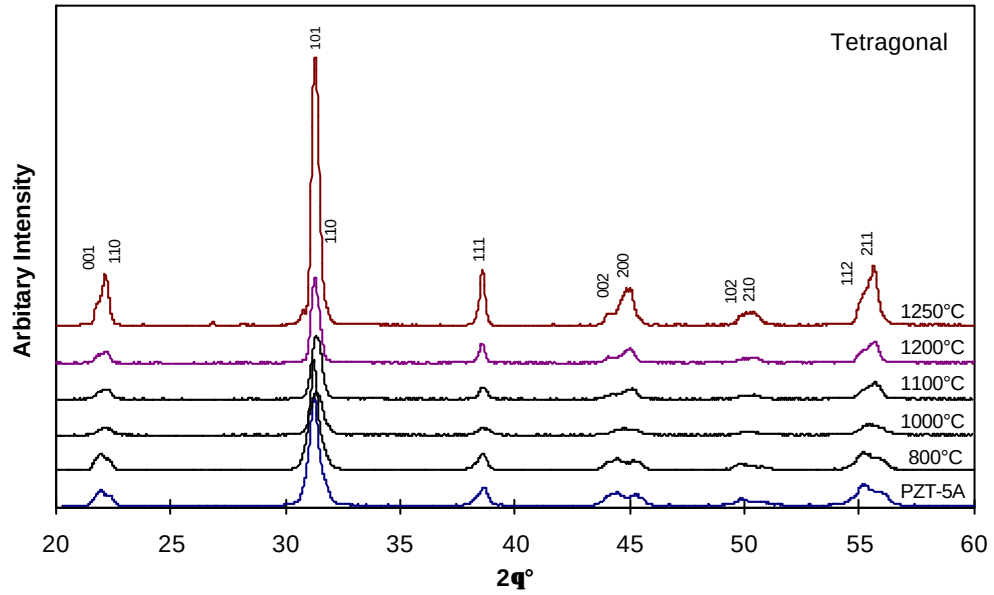

(b)

Fig. 7.21. XRD patterns of phase development of the (a) hydrothermal (HT-37) and (b) mixed-oxide (PZT-5A) PZT powders during sintering.

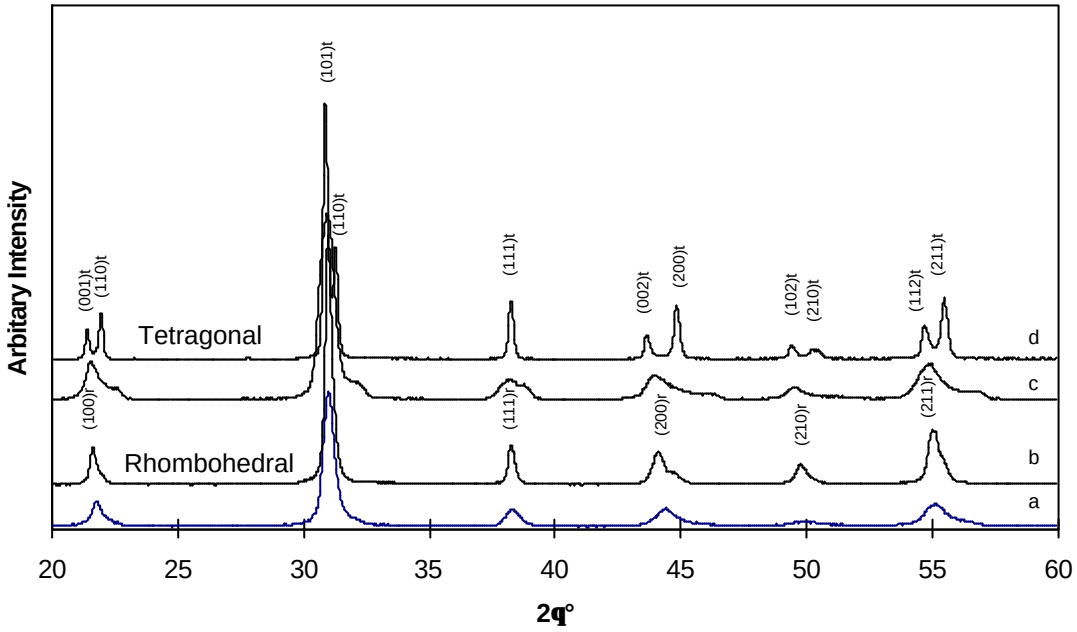

Fig. 7.22. XRD patterns of the HS-6 and HS-36 powders showing their different phase development on sintering at 1250°C for 1 hour: (a) as-synthesised HS-36 powder; (b) sintered HS-36 ceramic; (c) as-synthesised HS-6 powder; (d) sintered HS-6 ceramic. The HS-6 and HS-36 powders are synthesised at 200°C with a one-step-derived feedstock, using 2 M and 4 M KOH as the mineraliser, respectively.

Surface transport involves neck growth without a change in particle spacing (no densification) due to mass flow originating and terminating at the particle surface. Surface diffusion and evaporation-condensation are the two important contributors during surface transport-controlled sintering. In contrast, bulk transport-controlled sintering results in shrinkage. The mass originates at the particle interior with deposition at the neck. Bulk transport mechanisms include volume diffusion, grain boundary diffusion, plastic flow and viscous flow.

From the results presented in the previous sections, it can be seen that the hydrothermal PZT powders exhibit a quite different sintering behaviour compared to the mixed-oxide PZT powder. In particular, enhanced sinterability has been found for the PZT powders synthesised at the critical mineraliser concentration. This may be attributed to the different sintering mechanisms operating in the hydrothermal PZT powders as a consequence of the factors discussed below.

Firstly, the hydrothermal PZT powders generally possess a finer particle size and narrower particle size distribution (see Fig. 7.16), both of which facilitate uniform densification at lower sintering temperatures. Smaller particles exhibit faster neck growth due to their larger surface energy and need less sintering time or a lower sintering temperature to achieve an equivalent degree of sintering. This has been observed in many ceramic systems [German, 1996].

Secondly, the hydrothermal PZT powders synthesised at the critical concentration are not phase-homogenous, comprising a mixture of metastable PZT (T) and PZT (R) phases, as shown by the XRD and TEM (EDX) results (see Section 6.3). Thus, sintering of these powders occurs initially by a homogenisation and rearrangement densification process as shown by the XRD results (see Fig. 7.21 (a)), which probably accounts for its remarkable sinterability. A similar observation has been reported for conventional mixed-oxide powders in that enhanced densification of PZT could be achieved by only partially reacting the component powders [Venkataramani, 1981]. The enhanced densification is believed to be the result of an ‘activated’ sintering process accompanied by further

phase transformation during the final stage of perovskite formation, which is greatly beneficial to diffusion and the overall sintering process [Shrout *et al.*, 1990].

Finally, since no free lead oxide has been detected either by XRD and TEM (EDX) analysis, enhanced sintering by 'liquid phase sintering' [Snow, 1974] seems unlikely. However, the enhanced sintering behaviour could be attributed to a 'defect-activated sintering' mechanism, since the hydrothermal PZT powders synthesised at the critical mineraliser concentration are actually not well crystallised, and are likely to possess many lattice defects on both the particle surfaces and inside the particles induced by the residue groups such as acetate or hydroxyl group as shown in FT-IR result (Fig. 6.13) and TGA-DTA data (Fig. 7.14) in the present work, as well as reported in other hydrothermal synthesised ceramic powders [Noma *et al.*, 1996]. The energetic basis for sintering lies in the reduction of surface energy by transferring matter from the interior of grains along the grain boundaries to adjacent pores. During sintering, the most mobile entities are vacant crystal lattice sites which migrate from the pores into the grain boundaries, giving a reverse flow of mass into the pores. Densification occurs because the vacancies are annihilated at the interparticle grain boundaries, dislocations, phase boundaries, or other microstructural interfaces. An increase in defect concentration will, therefore, result in faster sintering [German, 1996]. Moreover, the weight loss due to lead oxide evaporation accompanying the initial sintering process results in the phase being non-stoichiometric and this generates Pb vacancies in the ceramics [Xu, 1991]. In a lattice having Pb vacancies, transfer of atoms is easier than in a perfect lattice; thus the sintering process is accelerated.

7.1.3.2. Microstructural evolution during sintering

The series of SEM micrographs of the fracture surfaces shown in Fig. 7.15 illustrate successive stages of the microstructural evolution during the sintering of uniaxially dry pressed compacts of both mixed-oxide (PZT-5A) and hydrothermal (HT-29) PZT powders. At a sintering temperature of 750°C, the microstructure for both PZT-5A and HT-29 powders has little change in comparison with their state in the green compacts. The HT-29 powder with finer particle size exhibits some coarsening without large agglomeration (Fig. 7.15 (a)), whereas the PZT-5A powder has some agglomerates surrounded by smaller particles (Fig. 7.15 (b)). When the sintering temperature is increased to 850°C, a tremendous change occurs for the HT-29 ceramic where sintering takes place rapidly with distinct grain boundaries visible on the fracture surface (Fig. 7.15 (c)), while for PZT-5A, only some particle agglomeration regions where the smaller particles surrounding larger ones begin sintering (Fig. 7.15 (d)). The density of the HT-29 increases markedly compared to that of the PZT-5A (see Fig. 7.11). This is because of the very fine, surface-active hydrothermal PZT powder, whose sintering is initially by a reactive homogenisation and rearrangement densification process, which accounts for its remarkable sinterability. As the sintering temperature is increased to 1000°C, the grain size of the HT-29 ceramic doubles from about 1 μm at 850°C to about 2 μm at 1000°C (Fig. 7.15 (e)), where the densification is by the conventional sintering mechanism governed by either lattice diffusion or grain-boundary diffusion. In contrast, the PZT-5A ceramic still undergoes intra-agglomerate sintering (Fig. 7.15 (f)). Finally, at the sintering temperature of 1200°C, the PZT-5A ceramic has sintered with clear grain boundaries on its fracture surface (Fig. 7.15(g)). Meanwhile, its density increases rapidly (Fig. 7.11), while the grain size of the HT-29 ceramic continues growing to about 2.8 μm (Fig. 7.15 (h)). The difference in the microstructure evolution between the hydrothermal HT-29 powder and the mixed-oxide PZT-5A powder is attributed to their different particle characteristics (Fig. 7.16). The finer particle size and narrower particle size distribution of the hydrothermal HT-29 powder facilitate uniform densification at lower sintering temperatures. As a result, the two ceramics exhibit entirely different sintering behaviours.

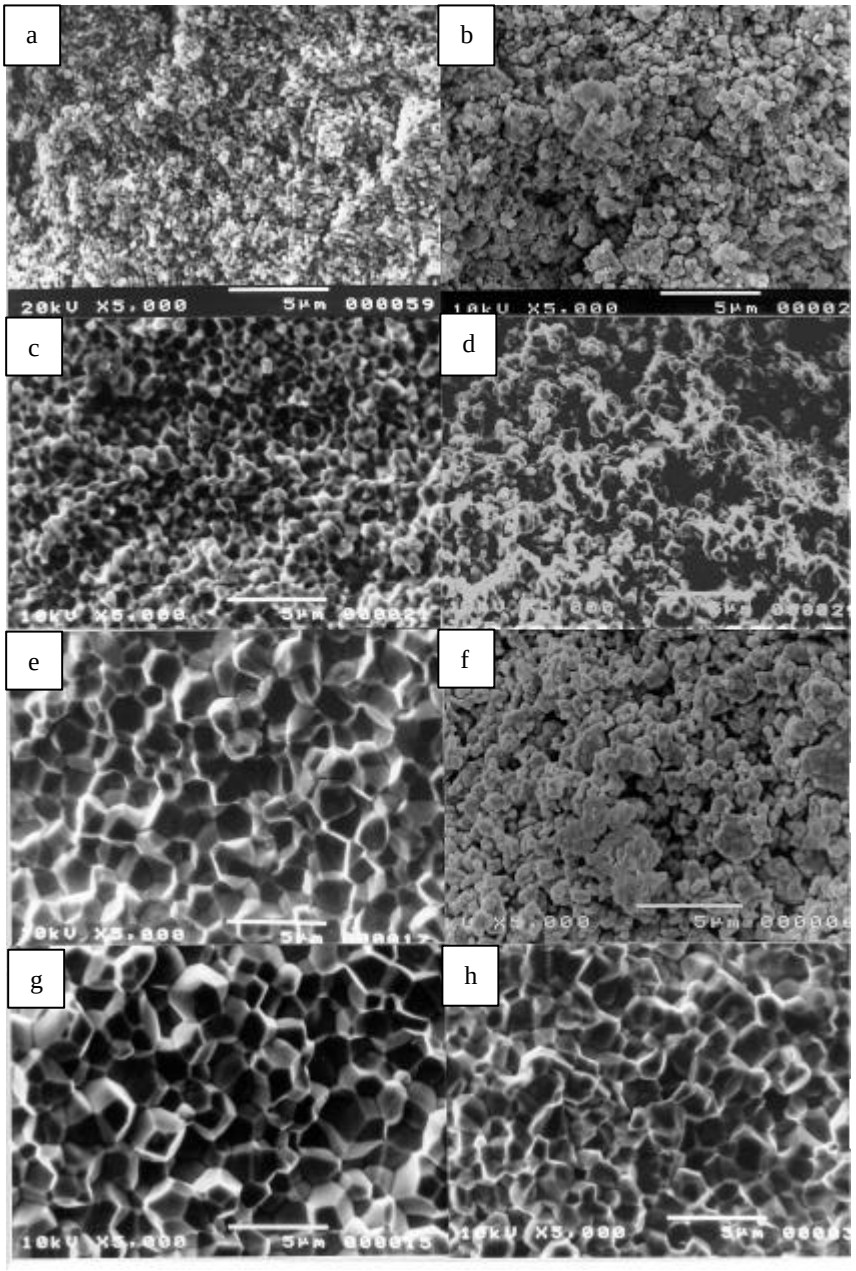

Fig. 7.15. SEM micrographs of the microstructural evolution of the fractured surfaces of PZT-5A and HT-29 ceramics during sintering showing the different sintering behaviour of PZT compacts under the same sintering conditions of (a) (b) 750°C; (c) (d) 850°C; (e) (f) 1000°C; and (g) (h) 1200°C for 2 hours, corresponding to the different powder characteristics.

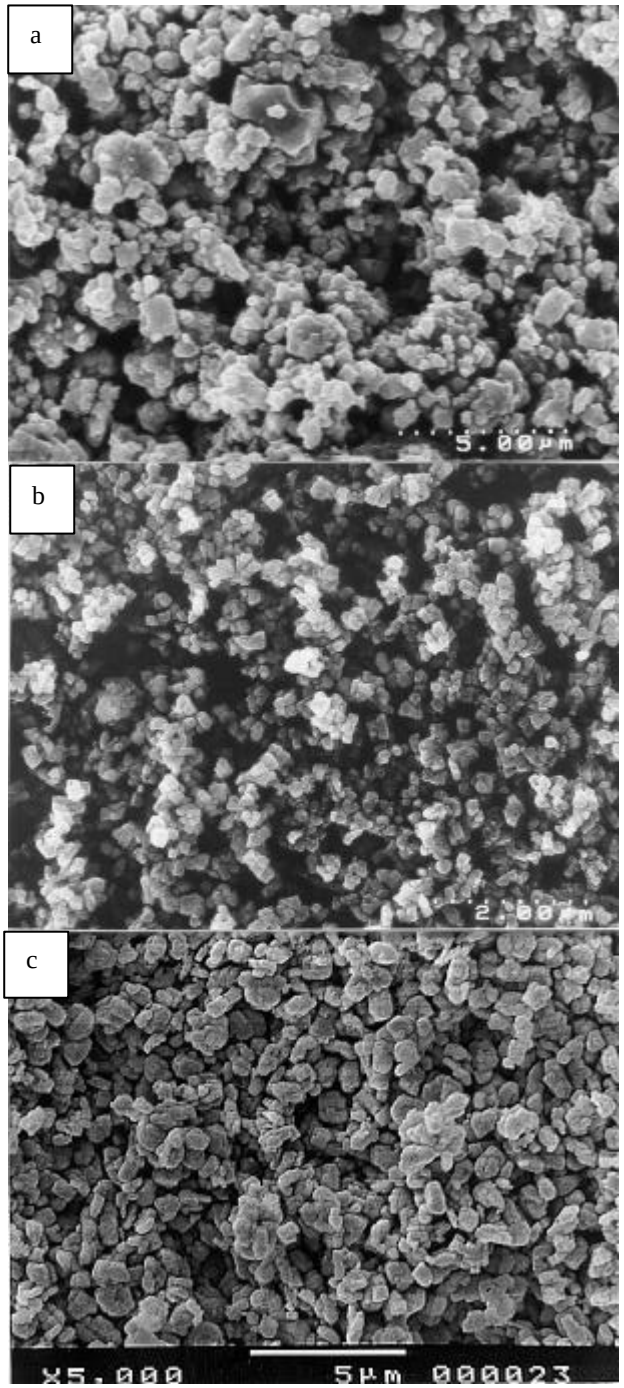

Fig. 7.16. SEM micrographs of the PZT powders: (a) mixed-oxide PZT-5A; (b) hydrothermal HT-29; and (c) hydrothermal HS-36 powder. Note that each powder exhibits different particle size distribution and morphology.

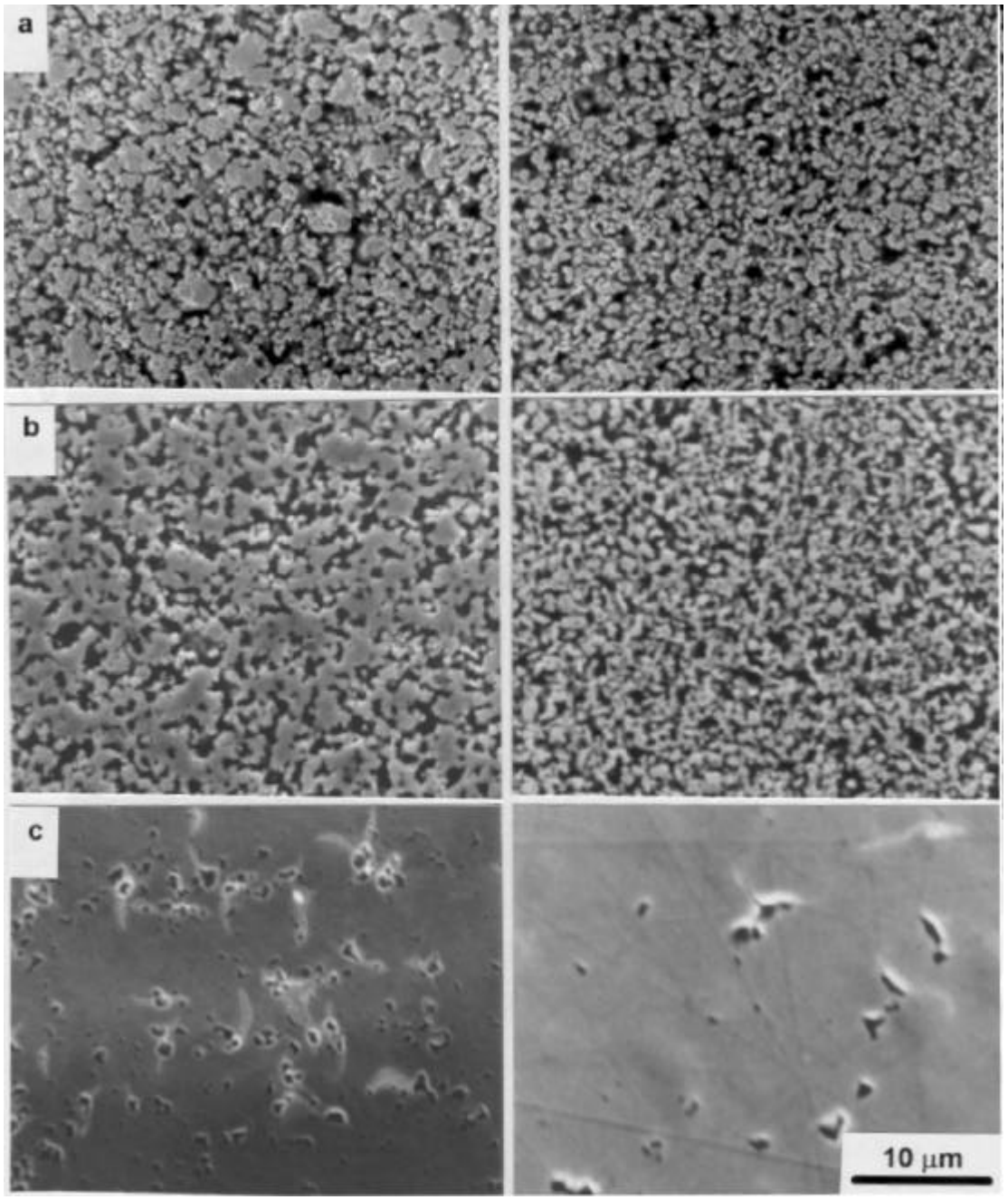

PZT-5A HS-36

Fig. 7.17. SEM micrographs of the microstructural evolution of PZT-5A and HS-36 ceramics during sintering showing the different sintering behaviour of PZT compacts under the same sintering conditions of (a) 1000°C; (b) 1100°C; and (c) 1250°C for 1 hour, corresponding to the different powder characteristics.

Fig. 7.17 shows the series of SEM micrographs of polished surfaces of the PZT-5A and another hydrothermal PZT powder, HS-36, which was synthesised at 200°C for 30 minutes using 4 M KOH as a mineraliser, together with the one-step derived feedstock. As can be seen from Fig. 7.16, both the average particle size and particle agglomeration for HS-36 are larger than that for PZT-5A, but the PZT-5A exhibits a broader particle size distribution. At a sintering temperature of 1000°C, for the PZT-5A powder, the particle agglomerate regions where the smaller particles are surrounding larger ones have sintered first (Fig. 7.17(a)). The PZT-5A powder with its smaller particle size portion shows a more significant effect on intra-agglomerate sintering. The difference in the agglomerate sizes becomes even more noticeable in the partially-sintered microstructures at a sintering temperature of 1100°C; see Fig. 7.17 (c). At this temperature, the partially-sintered microstructure of the HS-36 ceramic seems to be less developed than the PZT-5A. Finally, when the sintering temperature is raised to 1250°C, the density has increased dramatically for both ceramics. However, the microstructure change for the HS-36 ceramic is significant. No clear grain boundaries can be seen from its fracture surface, which has also been observed in other hydrothermal synthesised powders [Chan, 1997]. 'Viscous flow' during sintering seems responsible for such a phenomenon, especially for poorly-crystallised or amorphous materials [German, 1994]. The grain boundaries can only be seen on thermally-etched samples as shown in Fig. 7.18 (a). The densification of the PZT-5A seems via the conventional solid-state sintering mechanism where surface diffusion and grain boundary diffusion are dominant with the smaller particle sizes in crystalline materials [German, 1994]. The fully dense regions between the less dense regions promote grain growth, and thus increase the potential for forming larger grain microstructures in those systems containing larger particles and/or particle agglomerates. As can be seen from the thermally-etched sample of PZT-5A (Fig. 7.18 (b)), the final grain size of the fully dense microstructures reflects the size of the initial larger particles and particle agglomerates.

It is interesting to note that the thermal etching conditions have a marked effect on the appearance of the grain boundaries of the PZT ceramics due to volatilisation of PbO at temperatures above 800°C. The SEM micrographs in Fig. 7.18 (a) and (b) show that after thermal etching in air, the grain boundary structure is quite evident in the PZT-5A sample. In contrast, the HS-36 sample exhibits a porous structure with no distinct grain boundary structure. However, when thermal etched under the same conditions but in a PbO atmosphere buffer, both samples exhibit distinct grain boundary structures (see Fig. 7.18 (c) and (d)). Under the latter conditions, PbO evaporation is greatly suppressed; thus, these results are consistent with the previous observation that the PZT-5A ceramic is more stable against PbO loss and the hydrothermal PZT powders are probably PbO-rich on the surface and thus PbO-rich at the grain boundaries of the ceramics.

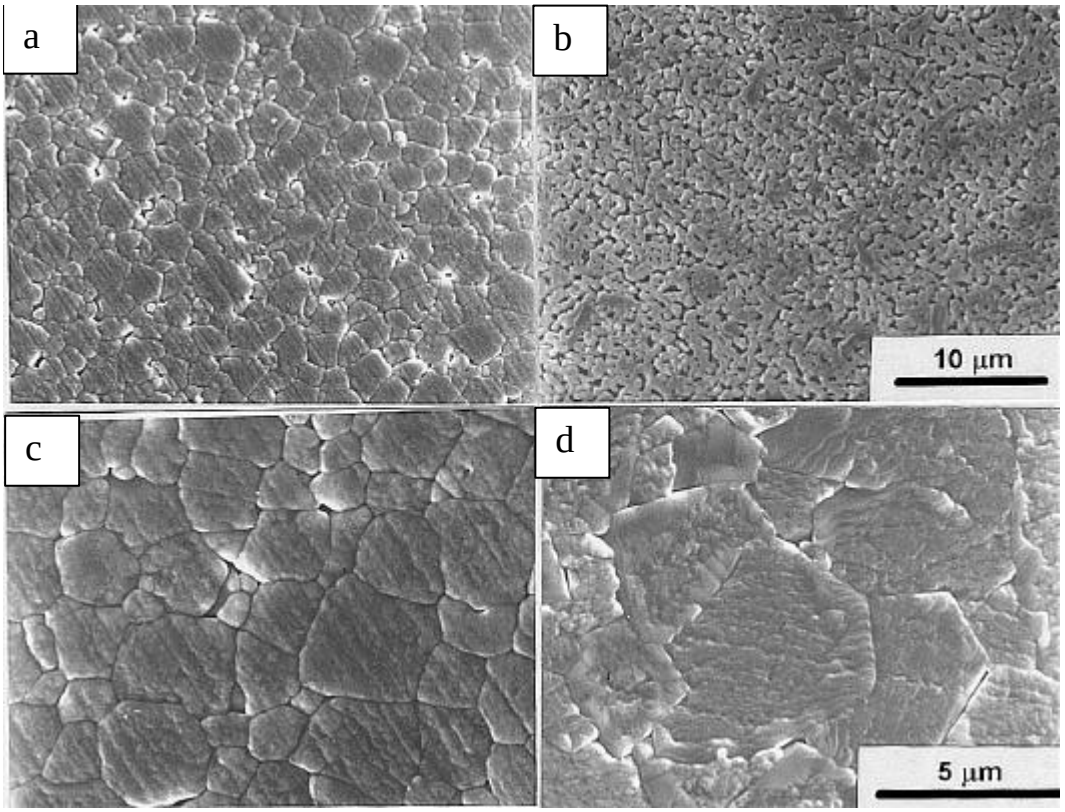

PZT-5A HS-36

Fig. 7.18. SEM micrographs of the thermally etched surfaces normal to pressing direction axis of the PZT-5A and HS-36 ceramics subjected to different atmospheres at 1000°C for 1 min: (a) air; (b) PZT buffer. Etching is clearly more severe in air.

The effect of sintering atmosphere is shown in Fig. 7.19. A higher sintered density and lower weight loss were observed for both the PZT-5A and HS-36 ceramics when sintered at 1250°C for 1 h in oxygen rather than in air. This is probably due to the higher O_2 partial pressure which suppresses the PbO volatilisation as shown by the lower weight loss in Fig. 7.19, and reduces the rate of grain growth as evident from Fig. 7.20. At higher grain growth rates, pores become trapped within grains, whereas at slower rates, the pores can diffuse out to the boundaries and be eliminated [Ogawa, 1991].

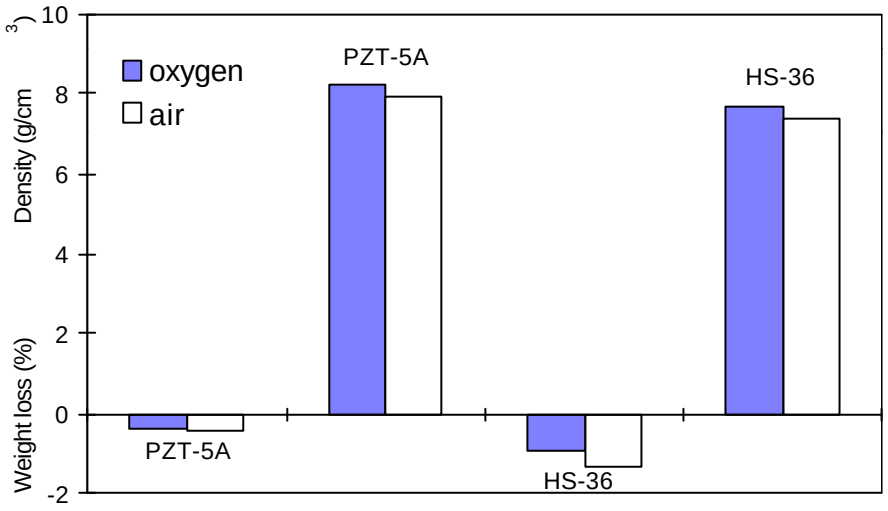

Fig. 7.19. Weight loss and density of the PZT-5A and HS-36 powders when sintering in different atmospheres.

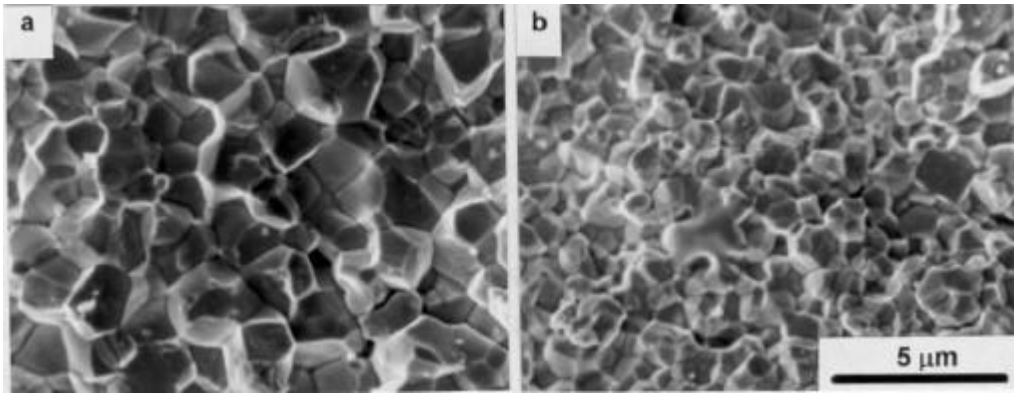

Fig. 7.20. Fracture surface of the PZT-5A ceramic sintered at 1250°C for 1h in (a) air and (b) an oxygen atmosphere.

Note the larger grain size on sintering in air.

7.1.4. Dielectric and Piezoelectric Properties

7.1.4.1. Effect of processing conditions

Unlike the mechanical properties of most structural ceramics, the electrical properties of PZT ceramics are not controlled by single defects but rather by the average microstructure, e.g. grain size, grain boundary composition and homogeneity. Many of these factors are determined by the processing conditions.

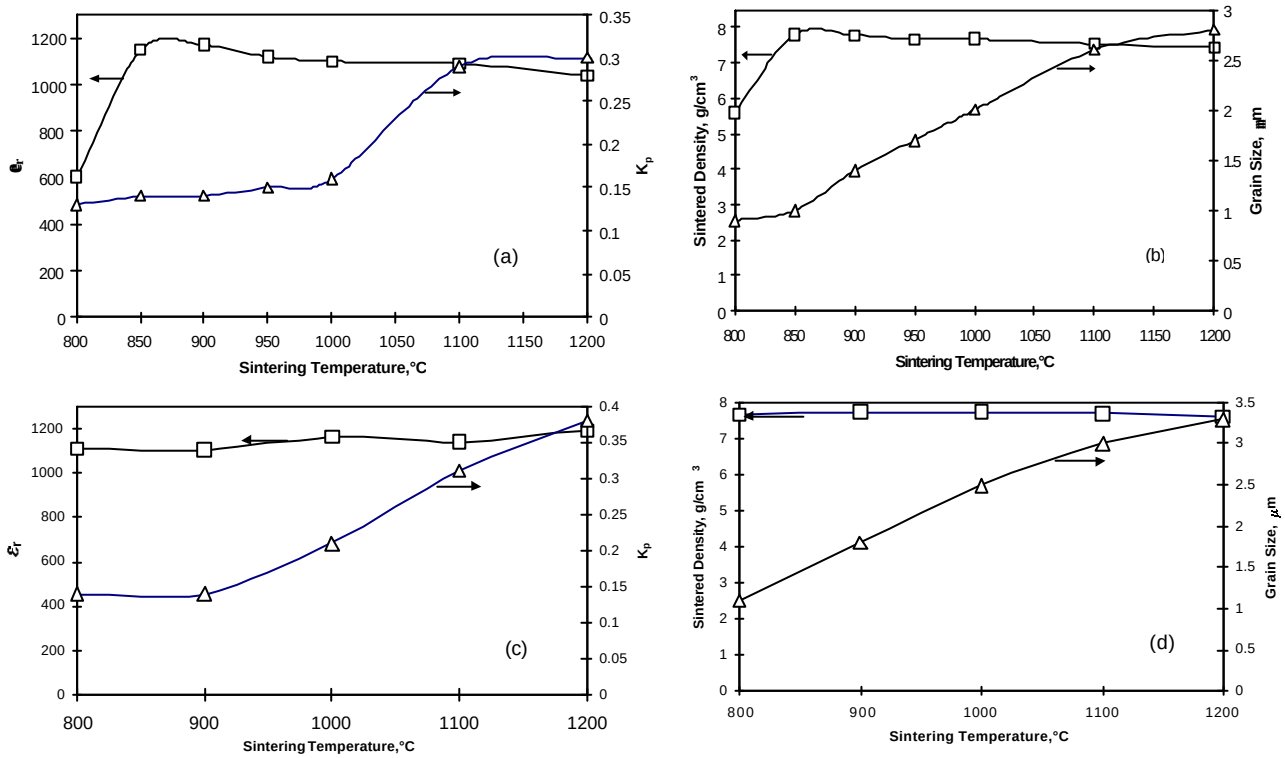

Fig. 7.23. Dielectric and piezoelectric properties together with sintered density and grain size changes of an undoped hydrothermal (HT-29) ceramic with the sintering temperature at different sintering times: (a) and (b) 5 minutes; (c) and (d) 2 hours.

Fig. 7.23 (a) shows the dielectric and piezoelectric properties, as represented by ε_r, the relative permittivity and K_p, the piezoelectric coupling coefficient, respectively, of an undoped hydrothermal PZT (HT-29) ceramic as a function of the sintering temperature at a short holding time of 5 minutes. Its corresponding sintered density and grain size changes are shown in Fig. 7.23 (b). It can be seen that the ε_r increases with the density, whereas the K_p seems to be more related to the grain size of the PZT ceramic. A maximum ε_r of about 1150 has been reached at 850°C, followed by a slight decrease due to the minor decrease of the density owing to the lead loss during sintering. The K_p, however, increases dramatically only when the grain size is above 1.8 μm. At a longer holding time of 2 hours, this trend is more obvious, where the ε_r almost keeps constant over the sintering temperature range (800°C to 1200°C) because of the high relative sintered density; the increase of K_p starts at about 900°C, where the grain size is about 1.8 μm, and increases steadily as the grain size increases (see Fig. 7.23 (c) and (d)). Since the K_p is more related to the mobility of the domain wall in the PZT ceramics, the increase of grain size results in more domains and, therefore, possibly more mobile walls [Martirena & Burfoot, 1974]. In ceramics with larger grain size, multi-domain effects accompanied by hysteresis are more likely to take place. Reduction in grain size lead to single-domain effects and, finally, at sufficiently small sizes, the number of domains is expected to diminish [Newhnam et al., 1992]. Mishra and Pandey [1995] reported that the formation of ferroelectric domains is not energetically favourable below a critical grain size. But this critical size is dependent on the material and its composition.

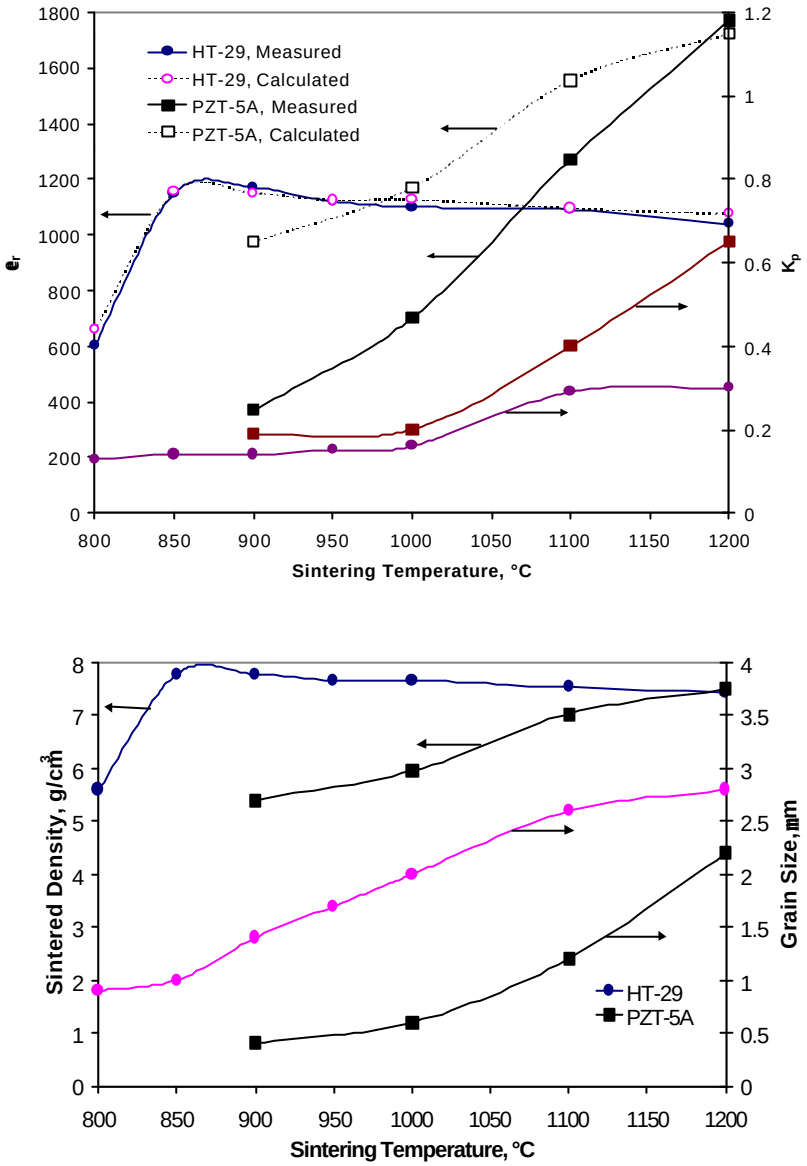

Fig. 7.24. Comparison of the electrical properties and microstructure changes of the undoped hydrothermal (HT-29) ceramic and the doped mixed-oxide (PZT-5A) ceramic as a function of the sintering temperature for a fixed sintering time of 5 minutes.

The dielectric property is a measurement of the polarizability which relates an induced dipole moment in an atom, ion, molecule etc., to the internal field inducing the dipole moment. Obviously, the dielectric property of a ferroelectric ceramic depends on both its intrinsic structure and its physical state. For a PZT ceramic with small inclusions of gas (porosity < 10 vol %), the relative permittivity obeys rules of mixture [Herbert, 1985]. The relation is as follows:

$$\varepsilon_r = \varepsilon_r' (1-3P/2) \qquad (7.1)$$

where ε_r and ε_r' is the relative permittivity of the ceramic with pores and fully dense form respectively and P is the porosity. Assuming the measured true density and the theoretical density of the PZT ceramic is ρ and ρ_{th}, respectively, then

$$\varepsilon_r = \varepsilon_r' [1-3(1-\rho/\rho_{th})/2] \qquad (7.2)$$

Fig. 24 shows the comparison of the ε_r and K_p change for the hydrothermal (HT-29) and mixed-oxide (PZT-5A) PZT ceramics during sintering process, the calculated ε_r are also shown in Fig. 7.24. It can be seen that the calculated and measured ε_r is only in agreement for the undoped HT-29. A large discrepancy has been found for the doped PZT ceramics (PZT-5A), which may be attributed to its relatively low density and thus high porosity at lower sintering temperatures. The difference of the K_p between the doped and undoped PZT ceramics is also evident; the increase in K_p for doped PZT ceramics starts at a lower grain size (i.e. 0.5 μm for the doped PZT-5A versus 1.8 μm for the undoped HT-29 ceramics). This implies that doping ions increases the domain wall mobility [Xu, 1991].

7.1.4.2. Effect of the doping

The electrical properties of sintered samples of both the mixed-oxide and hydrothermal PZT ceramics sintered at different conditions are given in Table 7.4.

Table 7.4. Electrical properties of sintered PZT ceramics.

Sample	**Composition**	**Sintering conditions**	**Density (g/cm^3)**	**K_p**	**ε_r**	**Q_m**
HT-29	$Pb(Zr_{0.52}Ti_{0.48})O_3$	1200°C/2 hours	7.49	0.42	989	147
HT-37	$Pb(Zr_{0.52}Ti_{0.48})O_3$ + 0.6 mol % Nb	1000°C/2 hours	7.51	0.55	1490	53
HT-34	$Pb(Zr_{0.52}Ti_{0.48})O_3$ + 1.0 mol % Nb	1100°C/2 hours	7.80	0.62	1610	48
HT-35	$Pb(Zr_{0.52}Ti_{0.48})O_3$ + 1.0 mol % La	1100°C/2 hours	7.43	0.60	1780	51
HS-36	$Pb(Zr_{0.52}Ti_{0.48})O_3$ + 3.0 mol % K	1200°C/2 hours	7.20	0.46	995	546
MO-PZT	$Pb_{1.01}(Zr_{0.52}Ti_{0.48})O_3$ + 2.0 mol % Nb	1200°C/2 hours	7.70	0.63	1700	46
PZT-5A	doped, unknown	1200°C/2 hours	7.71	0.65	1790	42

Comparing the electrical properties of the doped and undoped PZT ceramics in Table 7.4, we can see that (1) the K_p and ε_r values for the Nb or La doped PZT ceramics, whether from a mixed-oxide (e.g. MO-PZT) or hydrothermal synthesis (e.g. HT-37, HT-34, HT-35) route, are generally higher

than those of undoped PZT ceramics (e.g. HT-29, HS-36) and the K_p and ε_r values also seem to increase with increasing dopant content (HT-37, HT-34, MO-PZT), whereas their Q_m is generally lower than that of the undoped PZT ceramics; (2) the hydrothermal PZT ceramic (HS-36) with 3 mol % K residue has much higher Q_m than other PZT ceramics.

Above a certain sintered density, the K_p and ε_r is largely dependent on the composition of the PZT ceramics, i.e. reaching a maximum at the MPB with a Zr/Ti ratio of 52/48. The K_p values for the undoped HT-29 (0.42) and HS-36 (0.46) is in agreement with the literature at the MPB [Jaffe *et al.*, 1971].

When PZT ceramics are doped with "soft dopants" such as Nb or La in this study, the doping ions will either occupy the A-sites or B-sites to replace Pb^{2+} or Zr^{4+} and Ti^{4+} and create more Pb vacancies owing to their different valences. The Pb vacancies make the transfer of atoms easier than in a perfect lattice, thus increasing the domain wall mobility, as discussed in Section 2.3.2. Therefore, both K_p and ε_r are substantially higher, whereas the Q_m is lower in comparison with the undoped PZT ceramics.

The presence of potassium in the hydrothermal PZT ceramic (HS-36) is caused by unintentional contamination during the hydrothermal synthesis where KOH is used as a mineraliser. EDS analysis shows that a small amount of potassium is present within the hydrothermal PZT ceramics (about 1-3

mol %) depending on the feedstock preparation method and mineraliser concentration used, especially for PZT powders from one-step derived feedstock where a high mineraliser concentration is necessary for the perovskite PZT formation as discussed in Section 6.1.1. Potassium ions are known as hard dopants in PZT, which occupy the A sites in the perovskite structure, generating oxygen vacancies in the perovskite lattice as discussed in Section 2.3.2. Sintering the ceramic in an atmosphere of oxygen cannot eliminate these oxygen vacancies. This may explain the experimental observation that almost all the undoped PZT ceramics are dark grey in colour as reported in other ferroelectric ceramics with oxygen vacancies [Moulson & Herbert, 1991]. However, the perovskite structure is based on an oxygen octahedral framework. Thus, to maintain the stability of this framework, the oxygen vacancy concentration must be below a certain limit [Xu, 1991].

It has also been confirmed that PZT ceramics possess p-type conductivity, i.e. act as hole-type semiconductors [Gerson, 1960]. This is caused by PbO volatilisation from the PZT during sintering, which creates Pb vacancies in the sintered ceramic. A Pb vacancy can act as a centre of negative electric charge with an effective value of -2. One Pb vacancy, just like an acceptor impurity in semiconductors, offers an acceptor level and two holes, i.e.

$$\text{Pb vacancy} \rightarrow [\text{centre of negative charge}]^{2-} + 2\,[\text{holes}]^{+} \qquad (7.3)$$

Therefore, in a PZT ceramic with hard doping ions, the number density of space charges (i.e. both centres of negative charge and hole carriers) increases dramatically. These space charges cause an

internal electrical field inside the PZT grains, which may inhibit the movement of ferroelectric domain walls, resulting in the increase of Q_m [Takahashi, 1981].